Arabian Journal of Chemistry (2020) **13**, 8100–8118

King Saud University

Arabian Journal of Chemistry

www.ksu.edu.sa
www.sciencedirect.com

ORIGINAL ARTICLE

Structural, textural, morphological, magnetic and electromagnetic study of Cu-doped NiZn ferrite synthesized by pilot-scale combustion for RAM application

Elvia Leal [a,*], **Sabrina Trajano Basílio** [a], **Joelda Dantas** [a,b], **Priscila Richa** [c], **Roberto da Costa Lima** [c], **Ruth Herta Goldschmidt Aliaga Kiminami** [d], **Ana Cristina Figueiredo de Melo Costa** [a]

[a] *Academic Unit of Materials Engineering, Federal University of Campina Grande (UFCG), 882 Aprígio Veloso Ave, Bodocongó, 58429-900 Campina Grande, PB, Brazil*
[b] *Center of Alternative and Renewable Energies, Federal University of Paraíba (UFPB), Cidade Universitária, 58051-970 João Pessoa, PB, Brazil*
[c] *Navy Research Institute (IPQM), Materials Group/Chemical Technology Division, Ipiru 2 St, Ilha do Governador, 21931-095 Rio de Janeiro, RJ, Brazil*
[d] *Department of Materials Engineering, Federal University of São Carlos (UFSCar), Rod. Washington Luiz, Km 235, 13565-905 São Carlos, SP, Brazil*

Received 22 July 2020; accepted 21 September 2020
Available online 1 October 2020

KEYWORDS

Pilot-scale combustion;
NiZnCu ferrites;
Sintering;
Properties;
RAM application

Abstract The synthesis of the $Ni_{0.5\text{-}x}Zn_{0.5\text{-}x}Cu_{2x}Fe_2O_4$ (x = 0; 0.10 and 0.15) ferrite with the differential of pilot-scale production by the combustion reaction method was investigated for RAM application purposes. Combustion temperatures ranging from 682 °C to 738 °C were observed. All ferrites were sintered at 1200 °C for 1 h. A comprehensive study of the influence of substitution with Cu^{2+} in a partial and proportional way to the Ni^{2+} and Zn^{2+} ions, doping mode little reported in the literature, and also of the sintering process over the structural, textural, morphological, magnetic and electromagnetic properties of NiZnCu ferrites was performed. The XRD patterns of the ferrites as synthesized revealed the formation of the cubic structure of the inverse spinel as majoritary phase, and traces of hematite and zinc oxide as segregated phases. After sintering, it was proven the single-phase formation of cubic spinel ferrite structure. The introduction of Cu

---

* Corresponding author.
E-mail address: elvialeal@gmail.com (E. Leal).

Peer review under responsibility of King Saud University.

Production and hosting by Elsevier

https://doi.org/10.1016/j.arabjc.2020.09.041

led to a reduction in the lattice parameter, whose values ranged from 8.337 to 8.385 Å. The EDX results confirm the composition of oxides. The textural and morphological analyses confirmed the densest characteristic, with increase of particle size and reducing of surface area and pore volume after Cu-doping. All ferrites showed characteristics of soft ferrimagnetic material, where the increase in Cu content contributed to a slight reduction in saturation magnetization, whose values were of ~22–29 emu/g for the as synthesized ferrites and ~71–85 emu/g for the sintered ones. The best result of electromagnetic absorption in X-band was presented by the sintered ferrite with 0.3 mol of Cu, reaching an attenuation of 99.8% at 11.5 GHz frequency, thus confirming the efficiency of the pilot-scale combustion synthesis in obtaining a ferrite with great potential for RAM application.

1. Introduction

In recent years, the search for materials that are efficient for use as electromagnetic radiation absorbent materials (Naidu et al., 2017; Ali et al., 2018; Jafarian et al., 2019; Zhao et al., 2020), especially in the microwave absorption band, has advanced rapidly aiming at applications in electronic devices and communication instruments, whether for the commercial, industrial, scientific and/or military fields, such as, i.e., in mobile phones, computers, wireless networks systems and radar detection technologies, thus acting in the camouflage or shielding of highly reflective surfaces, as metallic surfaces, reducing the radar cross section (RCS) of targets, and eliminating problems of electromagnetic interference (EMI) and electromagnetic compatibility (EMC) (Zhou et al., 2020; Liu et al., 2019; Qin and Brosseau, 2012; Melvin et al., 2014).

An incident microwave is a coupling of an oscillatory electric field and magnetic field, then, the materials which promote microwave absorption are those that interact with either one of these two fields, or both, so to drive light/matter interaction at the gigahertz region of the electromagnetic (EM) spectrum (Green and Chen, 2019). This action is in accordance with Maxwell's equations, where the perturbation of one of the electromagnetic fields by interaction with a material medium will induce a response change of the other, resulting in the dissipation of the entire electromagnetic wave (Griffiths, 1999). Thus, the absorbed energy by the material is the energy component of the electromagnetic wave that undergoes the conversion of electromagnetic energy to thermal energy, due to the dielectric (complex permittivity) and magnetic (complex permeability) properties of the material.

Ferrites have aroused interest for being a promising material for use as absorbers of electromagnetic radiation at high frequency range because they present high saturation magnetization and large Snoek's limit, which lead to high permeability values over the GHz region (Liu et al., 2017a). In addition, as ferrites are considered magnetic materials, they have considerable electromagnetic radiation absorption capacity through the hysteresis loss mechanism, domain wall resonance and eddy (Foucault) current effect (Liu et al., 2017a, 2017b, 2017c). Spinel-type ferrites have a $MeFe_2O_4$ molecular formula, where Me is the divalent ion (Mg^{2+}, Mn^{2+}, Co^{2+}, Ni^{2+}, Cu^{2+}, Zn^{2+}, Cd^{2+}) and Fe^{3+} is the trivalent ion. More specifically, NiZn ferrites, which have an inverse spinel type structure, formed by a nearly close packed face centered cubic (FCC), since they have holes formed by an array of anions that are partially filled with cations, which can be represented by the formula $(Zn_xFe_{1\text{-}x})[Ni_{1\text{-}x}Fe_{1+x}]O_4$, in which Zn^{2+} ions are located in the tetrahedral sites (A), Ni^{2+} ions in the octahedral sites (B), and Fe^{3+} ions can occupy both the tetrahedral and octahedral sites in the spinel lattice (Peng et al., 2011). In recent years, NiZn ferrites among other ferrites have been considered as soft magnetic material with great potential for application in high frequency devices (such as multilayer chip inductors and electromagnetic interference filters) due to their high values of chemical stability, magnetization, Curie temperature, resistivity, permeability and low energy loss at high frequencies (Guo et al., 2020; Gao et al., 2013; Aphesteguy et al., 2009).

In ferrites as a whole, an effective means of obtaining good chemical, magnetic and microwave-absorbing properties is by means doping with other chemical elements (Wang et al., 2017; Zhou et al., 2019; Liu et al., 2019; Kabbur et al., 2019; Gabal and Al-Juaid, 2020). NiZn ferrite, in turn, can have its attributes considerably improved by the doping of divalent ions such as Co^{2+}, Cu^{2+}, Mn^{2+}, among others. Among these dopants, particularly, Cu^{2+} ions present an interesting crystallographic occupation in the NiZn ferrite due to its preferential occupation in the octahedral sites (B), which causes distortions in the tetragonal structure according to the Jahn-Teller effect (Parfenov et al., 2003). In the case of NiZnCu ferrites, the vast majority of studies focus on the partial substitution of Ni^{2+} ions by Cu^{2+} ions in the NiZn ferrite crystalline lattice (Das and Singh, 2016; Dantas et al., 2017; Lima et al., 2008; Aphesteguy et al., 2009; Barba et al., 2020), others report the substitution of Zn^{2+} ions (Venkatesh and Ramesh, 2017; Venkatesh et al., 2020), and almost nothing is found in the literature about the partial and proportional substitution of both Ni^{2+} and Zn^{2+} ions by Cu^{2+} ions, as shown at the present study as differential ($Ni_{0.5\text{-}x}Zn_{0.5\text{-}x}Cu_{2x}Fe_2O_4$). These substitutions, therefore, have an important role on the microstructure, intrinsic properties, atomic diffusivity, and even on the sintering kinetics of these ferrites. Cu when introduced in NiZn ferrite allows to improve properties such as initial permeability, electromagnetic properties, electrical resistivity, and chemical stability at high frequencies (Hossen and Hossain, 2015; Jia et al., 2012; Sujatha et al., 2013).

However, the final state of the magnetic and electromagnetic properties of these ferrites depends strongly on the characteristics of the particles and microstructure after the calcination and/or sintering process. It is known that small particles have high free surface energy, which allows to obtain higher density values at low temperatures of calcination and sintering (Das and Singh, 2016). As the microstructure and magnetic properties of ferrites are very sensitive to the synthesis method, and many of these routes are not commercially viable due to disadvantages such as high complexity, long synthesis time or penetration of impurities, the use of wet chemical methods is desirable since it allows greater phase homogeneity, smaller particle sizes and good magnetic characteristics (Dantas et al., 2020; Leal et al., 2018; Li et al., 2019). Among the wet chemical methods that have been adopted for the synthesis of NiZnCu ferrite nanoparticles, it can mention the hydrothermal (Praveena et al., 2016), sol–gel (Hashim et al., 2018), coprecipitation (Virlan et al., 2020), sonochemical (Slimani et al., 2020), and combustion methods (Dantas et al., 2017). In the present study, it was adopted the combustion reaction method, since it is a simple, fast (few minutes of reaction), and economical technique, which allows an excellent reproducibility of the formed products in terms of microstructure, and which, in function of the adopted conditions of synthesis, can produce powders with particle sizes ranging from nano to micron scale. Furthermore, as differential of this work, the combustion reaction method was adopted for the production of NiZnCu ferrite at pilot-scale, which allows a better perspective for future technological applications, either as radar absorbing materials (RAM), focus of the present study; biomaterials, catalysts, among others.

Therefore, this work aims to evaluate the effect of sintering and Cu-doping on NiZn ferrite obtained by the combustion reaction method at pilot-scale of 200 g/batch, and its relationship with structural, textural, morphological, magnetic and electromagnetic properties, aiming to obtain electromagnetic radiation absorbing materials that can operate at frequency range from 8.2 to 12.4 GHz (X-band). This work also seeks to contribute to the discovery of new compositions of the NiZnCu ferrite, since, unlike the vast majority of current research, the Cu^{2+} ions partially and proportionally replace the Ni^{2+} and Zn^{2+} ions amid the structure of NiZn spinel ferrite ($Ni_{0.5\text{-}x}Zn_{0.5\text{-}x}Cu_{2x}Fe_2O_4$).

2. Experimental

2.1. Synthesis of the ferrites

For the synthesis by combustion reaction of the $Ni_{0.5\text{-}x}Zn_{0.5\text{-}x}Cu_{2x}Fe_2O_4$ (x = 0; 0.10 and 0.15 mol of Cu^{2+}) ferrites, the following reagents were used to form the redox solution: nickel nitrate hexahydrate - $Ni(NO_3)_2{\cdot}6H_2O$ (Vetec, 98%), zinc nitrate hexahydrate - $Zn(NO_3)_2{\cdot}6H_2O$ (Vetec, 97%), copper nitrate trihydrate - $Cu(NO_3)_2{\cdot}3H_2O$ (Vetec, 98%) and iron(III) nitrate nonahydrate - $Fe(NO_3)_3{\cdot}9H_2O$ (Vetec, 99%) that acted as oxidizing agents and source of cations, and urea - $CO(NH_2)_2$ (Vetec, 97%) as fuel and reducing agent.

In the process of synthesis of the $Ni_{0.5\text{-}x}Zn_{0.5\text{-}x}Cu_{2x}Fe_2O_4$ magnetic nanoparticles by combustion reaction, the proportion of mixture of each reagent was calculated based on the thermodynamic concepts of the chemistry of propellants and explosives (Jain et al., 1981), taking into account the valences of the reactive elements as being: Ni = 2; Zn = 2; Cu = 2; Fe = 3; C = 4; H = 1; N = 0, and O = -2. In ferrites, Cu can assume the valences Cu^{1+} and Cu^{2+}, however, the valence state '+2', as it is more stable in the spinel lattice, was adopted for the discussions of this work. Ergo, the oxidizing valence of the divalent metallic nitrate, $M(NO_3)_2$, becomes −10; the trivalent metal nitrate, $M(NO_3)_3$, becomes −15; and the reducing valence of the urea fuel, $CO(NH_2)_2$, becomes + 6. Therefore, for a maximum energy release, considering the stoichiometric composition of the redox mixture (Φe = 1), all oxygen content from the metal nitrates must oxidize in an equivalent way all the fuel present in the mixture, that is, leading to an oxygen balance equals zero (OB = 0) (Hwang et al., 2005). So, considering that it is a MFe_2O_4 spinel-type ferrite, where 1 mol of M (−10), plus 2 mol of Fe (−15), requires an equivalent amount of 'n' moles of fuel, that is, $[1 \times (-10) + 2 \times (-15) + n \times (+6)] = 0$, n = 40/6 = 6.67 mol of urea. Based on this, the chemical reactions for the syntheses of the $Ni_{0.5\text{-}x}Zn_{0.5\text{-}x}Cu_{2x}Fe_2O_4$ (x = 0; 0.10 and 0.15) system can be expressed in a simplified way as shown below:

(a) For x = 0, $Ni_{0.5}Zn_{0.5}Fe_2O_4$:

$$\begin{aligned}&0.5{\cdot}\mathrm{Ni(NO_3)_2{\cdot}6H_2O_{(s)}} + 0.5{\cdot}\mathrm{Zn(NO_3)_2{\cdot}6H_2O_{(s)}}\\&+ 2Fe(NO_3)_3 \cdot 9H_2O_{(s)} + 6.67 \cdot CO(NH_2)_{2(s)}\\&\rightarrow Ni_{0.5}Zn_{0.5}Fe_2O_{4(s)} + 6.67 \cdot CO_{2(g)}\\&+ 37.33 \cdot H_2O_{(g)} + 10.67 \cdot N_{2(g)}\end{aligned}$$

(b) For x = 0.10, $Ni_{0.4}Zn_{0.4}Cu_{0.2}Fe_2O_4$:

$$\begin{aligned}&0.4{\cdot}\mathrm{Ni(NO_3)_2{\cdot}6H_2O_{(s)}} + 0.4{\cdot}\mathrm{Zn(NO_3)_2{\cdot}6H_2O_{(s)}}\\&+ 0.2 \cdot Cu(NO_3)_2 \cdot 3H_2O_{(s)} + 2Fe(NO_3)_3 \cdot 9H_2O_{(s)}\\&+ 6.67 \cdot CO(NH_2)_{2(s)} \rightarrow Ni_{0.4}Zn_{0.4}Cu_{0.2}Fe_2O_{4(s)}\\&+ 6.67 \cdot CO_{2(g} + 36.73 \cdot H_2O_{(g)} + 10.67 \cdot N_{2(g)}\end{aligned}$$

(c) For × = 0.15, $Ni_{0.35}Zn_{0.35}Cu_{0.3}Fe_2O_4$:

$$\begin{aligned}&0.35{\cdot}\mathrm{Ni(NO_3)_2{\cdot}6H_2O_{(s)}} + 0.35{\cdot}\mathrm{Zn(NO_3)_2{\cdot}6H_2O_{(s)}}\\&+ 0.3 \cdot Cu(NO_3)_2 \cdot 3H_2O_{(s)} + 2Fe(NO_3)_3 \cdot 9H_2O_{(s)}\\&+ 6.67 \cdot CO(NH_2)_{2(s)} \rightarrow Ni_{0.35}Zn_{0.35}Cu_{0.3}Fe_2O_{4(s)}\\&+ 6.67 \cdot CO_{2(g)} + 36.43 \cdot H_2O_{(g)} + 10.67 \cdot N_{2(g)}\end{aligned}$$

The redox mixtures of metallic nitrates plus fuel were submitted to direct heating in a conical reactor of stainless steel coupled with electrical resistance and with a production capacity of 200 g/batch, which was designed for combustion reaction synthesis in pilot-scale, as described at the patent BR 10 2012 002181-3 (Costa and Kiminami, 2012). The product of each reaction, obtained in the form of friable flakes, was deagglomerated in a porcelain mortar and sieved in a mesh #325 ABNT (45 μm), as shown in Fig. 1. The samples were sintered at 1200 °C/1h with heating rate of 10 °C/min in a muffle oven model Jung 1400.

During the syntheses, the reaction temperature was measured at 5 s time intervals, in online way, using an infrared pyrometer model RAYR3I ± 2 °C, Raytek. The total reaction time and the flame time were measured using a Technos® digital timer. To simplify the nomenclatures, the obtained ferrite systems were denominated: NZ ($Ni_{0.5}Zn_{0.5}Fe_2O_4$), NZC2 ($Ni_{0.4}Zn_{0.4}Cu_{0.2}Fe_2O_4$) and NZC3 ($Ni_{0.35}Zn_{0.35}Cu_{0.3}Fe_2O_4$) for the ferrites as synthesized; and NZ-12 ($Ni_{0.5}Zn_{0.5}Fe_2O_4$), NZC2-12 ($Ni_{0.4}Zn_{0.4}Cu_{0.2}Fe_2O_4$) and NZC3-12 ($Ni_{0.35}Zn_{0.35}Cu_{0.3}Fe_2O_4$) for the ferrites sintered at 1200 °C/1h.

Fig. 1 Combustion synthesis (a) and beneficiation process (b) of the reaction products.

2.2. Characterization techniques

The samples were characterized by X-ray diffraction (XRD) on a diffractometer from Bruker, model D2 Phaser, with CuKα radiation (λ = 1.5418 Å), an angle ranging from 10 to 70° (2θ), voltage of 40 kV and current of 30 mA. The crystallinity and crystallite size for the main peak (3 1 1) were calculated from the DIFFRAC.EVA software which is based on Debye-Scherrer's equation (Klug and Alexander, 1954). The lattice parameter (a) was calculated for each composition using Eq. (1) (Krishna et al., 2012):

$$a = d_{hkl}(h^2 + k^2 + l^2)^{1/2} \tag{1}$$

where a is the lattice constant; d_{hkl} is the inter planar distance; and (h, k, l) are the Miller indices.

And the theoretical lattice parameter (a_{th}) was calculated taking into account the proportion of each element present in the composition of NiZnCu ferrite, and using the following the relation (Eq. (2)) (Bajorek et al., 2019; Mapossa et al., 2020):

$$a_{th} = \frac{8}{3\sqrt{3}} \cdot \left[(r_A + r_O) + \sqrt{3}.(r_B + r_O)\right] \tag{2}$$

where r_A and r_B are the theoretical ionic radius of a tetrahedral and an octahedral sites, respectively, and r_O is de radios of oxygen ion (1.32 Å). The values of r_A and r_B may be calculated from the relations described by the Eqs. (3) and (4) (Bajorek et al., 2019):

$$r_A = C_{AZn}.r(Zn^{2+}) + C_{AFe}.(Fe^{3+}) \tag{3}$$

$$r_B = \frac{1}{2} \cdot \left[C_{BNi}.r(Ni^{2+}) + C_{BCu}.r(Cu^{2+}) + C_{BFe}.(Fe^{3+})\right] \tag{4}$$

where C_{ANi}, C_{AFe}, C_{BNi}, C_{BCu}, C_{BFe} represents the concentration of Zn^{2+}, Fe^{3+} at A-tetrahedral sites and Ni^{2+}, Cu^{2+}, Fe^{3+} at B-octahedral sites, respectively, whereas r denotes ionic radii for appropriate ions Zn^{2+} (0.74 Å), Fe^{3+} (0.64 Å), Ni^{2+} (0.69 Å) and Cu^{2+} (0.73 Å) (Houshiar and Jamilpanah, 2018).

Furthermore, the X-ray density (d_{XRD}) was determined using Eq. (5) (Deepty et al., 2019; Krishna et al., 2012):

$$d_{XRD} = \frac{Z.MW}{N_A.a^3} \tag{5}$$

where Z is the number of molecules per unit cell (Z = 8), MW is the molecular weight, N_A is the Avogadro's number and a is the experimental lattice constant. The experimental density (d_{EXP}) was determined by helium (He) gas pycnometry from Quantachrome Corporation, model Upyc 1200e v5.04 Pycnometer. The relative density (d_{REL}) was calculated using the relation described by Eq. (6):

$$d_{REL} = \frac{d_{EXP}}{d_{XRD}} \tag{6}$$

The semi-quantitative analysis of the oxides and elements present in the ferrite samples was determined by energy dispersive X-ray fluorescence spectroscopy (EDX) using an equipment from Shimadzu, model EDX-720. The theoretical percentage values of the oxides constituting the $Ni_{0.5\text{-}x}Zn_{0.5\text{-}x}Cu_{2x}Fe_2O_4$ ferrite were determined using Eq. (7):

$$\%X_O = \frac{M_O}{M_T}.100 \tag{7}$$

where X_O is the theoretical percentage of the oxide in question (NiO, ZnO, CuO or Fe_2O_3), M_O is the molecular mass of this oxide (g) and M_T is the total molecular mass of the analyzed ferrite (g).

The textural analysis of the ferrite samples was determined using a surface area analyzer with micropore analysis station, model Autosorb iQ, Quantachrome. The surface area (S_{BET}) was determined according to the method developed by Brunauer, Emmett and Teller (BET) based on nitrogen gas adsorption at multilayers. The particle sizes (equivalent spherical diameters) (D_{BET}) were calculated by Eq. (8) (Reed, 1995). The pore volumes (V_P) and pore diameters (D_P) were determined according to the theory developed by Barrett, Joyner and Halenda (BJH).

$$D_{BET} = \frac{6}{d_{EXP}.S_{BET}} \tag{8}$$

where D_{BET} is the equivalent average diameter (nm), S_{BET} is the surface area (m^2/g), d_{EXP} is the experimental density determined by pycnometry (g/cm^3) and the number '6' is an experimentally calculated factor that represents particles with approximately spherical shape and no roughness.

The morphological aspects of the ferrites samples were investigated using a scanning electron microscope (SEM), model XL30 FEG, Philips.

The magnetic properties of the samples were evaluated using a vibrating sample magnetometer (VSM), model 7404 by Lake Shore, with a maximum magnetic field of 13.700 G at room temperature. By means of the M × H hysteresis loops it was possible to determine some magnetic parameters, such as the coercive field (Hc), remnant magnetization (M_R), saturation magnetization (M_S) and remanence ratio (M_R/M_S). The values of Bohr magneton (n_B) were calculated using Eq. (9) (Satpute et al. 2019).

$$n_B = \frac{MW.M_S}{5585} \tag{9}$$

where MW is the molecular weight and M_S is the saturation magnetization obtained from the hysteresis loop.

The investigation of the electromagnetic microwaves absorption at frequencies range of 8.2–12.4 GHz (X-band) was carried out using specimens of ferrite/paraffin with weight ratio of 50/50 w/w, which were tightly inserting into a rectangular waveguide and analyzed by the Transmission/Reflection method (T/R) (Baker-Jarvis et al., 1993). The measurements of the microwave reflectivity level were determined by measuring variations of the reflection loss (dB) versus frequency (GHz) using a network analyzer system, model N5232A PNA-L, Keysight. The equations that relate the scattering data to the permeability (μ′, μ″) and permittivity (ε′, ε″) of the samples follow the Nicolson-Ross-Weir algorithm (Nicolson, 1968; Costa et al., 2017). The waveguide sample holder ($22.86 \times 10.16\ mm^2$) was fabricated by cutting the flange from an X-band standard waveguide with 8 mm in length. The measurement calibration procedure adopted typical waveguide standards: a $\lambda_{gm}/4$ off-set (line), a short circuit (reflect), and a 'thru' measurement (where λ_{gm} is the guided wavelength at the geometric mean frequency for the X-band). In order to avoid undesirable resonances during the measurements, the thickness of the samples was limited to 1.0–2.0 mm.

3. Results and discussion

3.1. Combustion synthesis parameters

When chemical elements are added in a combustion reaction, their atomic emission spectra can affect the frequencies of visible light radiation emitted, in other words, the flame appears in different colors according to the chemical element added. Then, in the heating of a reaction, the outermost electrons of the chemical elements present in the molecules of the reagents, tend to get more excited, gaining energy to jump to more internal electronic levels (high energy levels). Since this new energy state is unstable, these electrons tend to quickly return to their lowest energy state, thus releasing an energy photon with a wavelength equivalent to the difference of these energy levels. As the emission spectrum is unique for each element, it is common that in combustion flames, copper (II) emits photons in green color, zinc (II) in bluish-green to pale green color, nickel (II) in white color or colorless, and iron (III) in orange-brown color (Conkling and Mocella, 2010).

Fig. 2 shows images of the combustion flames captured during the syntheses by combustion reaction of the NZ ($Ni_{0.5}Zn_{0.5}Fe_2O_4$), NZC2 ($Ni_{0.4}Zn_{0.4}Cu_{0.2}Fe_2O_4$) and NZC3 ($Ni_{0.35}Zn_{0.35}Cu_{0.3}Fe_2O_4$) ferrites, respectively. It is possible to observe intense flames, with heights of approximately 1 m (1 m). As expected, the combustion flame referring to the undoped NiZn ferrite synthesis prevailed in the orange color from iron element, while in the compositions of the Cu-doped NiZn ferrites, as this dopant was added, the flames gained tonalities more for the green color.

Fig. 3 shows the temperature curves as a function of time measured during the syntheses by combustion reaction of the $Ni_{0.5-x}Zn_{0.5-x}Cu_{2x}Fe_2O_4$ (x = 0; 0.10 and 0.15) nanoferrites. And at Table 1 are the reaction parameters from the combustion syntheses, such as maximum temperature reached during the reaction (T_{max}), total reaction time (t_r), flame time (t_f), total mass of the reaction product (m), and color of the combustion flame.

According to Fig. 3, small fluctuations in temperature can be observed throughout the interval preceding ignition. This occurs due to the dehydration of nitrates in the presence of the fuel, which leads to a great release of gases and an increase in the viscosity of the mixture, providing, in sequence, the ignition. As expected, the temperature of the combustion flame increases substantially shortly after ignition, reaching the maximum reaction temperature, which ranged from 682 to 738 °C. It was also observed that as the copper content in the system increased, the lower the maximum combustion temperature reached, going from 738 °C at NZ ferrite synthesis, to 702 °C at NZC2, and 682 °C at NZC3. However, it can be said that the values presented were very close, with a maximum variation of only 56 °C.

According to Table 1, it is observed that the syntheses presented flame times ranging from 18 to 24 s, with the maximum value for the synthesis of NZC2 ferrite; total reaction time not exceeding 17 min; and total mass of the reaction product ranging from 209 to 215 g, that is, a production above expectations, since the synthesis reactor was designed for a maximum production capacity of 200 g/batch (Costa and Kiminami, 2012).

Therefore, it is possible to affirm the success of the combustion syntheses in the ferrites production at pilot-scale, and that these synthesis parameters are intrinsic characteristics of each system, having great relevance at determining the properties and characteristics of the final product (Dantas and Costa, 2019).

3.2. Structural characterization

Fig. 4 shows the X-ray diffraction curves referring the $Ni_{0.5-x}Zn_{0.5-x}Cu_{2x}Fe_2O_4$ (x = 0; 0.10 and 0.15) ferrites as synthesized and sintered at 1200 °C/1h. It is observed at the X-ray diffractograms of the as synthesized $Ni_{0.5-x}Zn_{0.5-x}Cu_{2x}Fe_2O_4$ ferrites (Fig. 4a), that the combustion reaction method at pilot-scale allowed the formation of the cubic structure of the inverse spinel ferrite, evidenced by the positions and relative intensities of the 8 (eight) main peaks referring to the (1 1 1), (2 2 0), (3 1 1), (2 2 2), (4 0 0), (4 2 2), (5 1 1) and (4 4 0) planes of spinel ferrites, which are close fitted to the standard JCPDS file no. 48-0489, indicating Fd3m space group. All diffractograms also showed the presence of less intense peaks characteristic of the segregated phase of hematite (Fe_2O_3), according to standard JCPDS file no. 25-1228. Besides hematite, the diffractograms of NZ and NZC3 samples also showed the presence of the segregated phase of zinc oxide (ZnO) identified by the standard JCPDS file no. 79-0208. Kabbur et al. (2018) when analyzing by XRD the

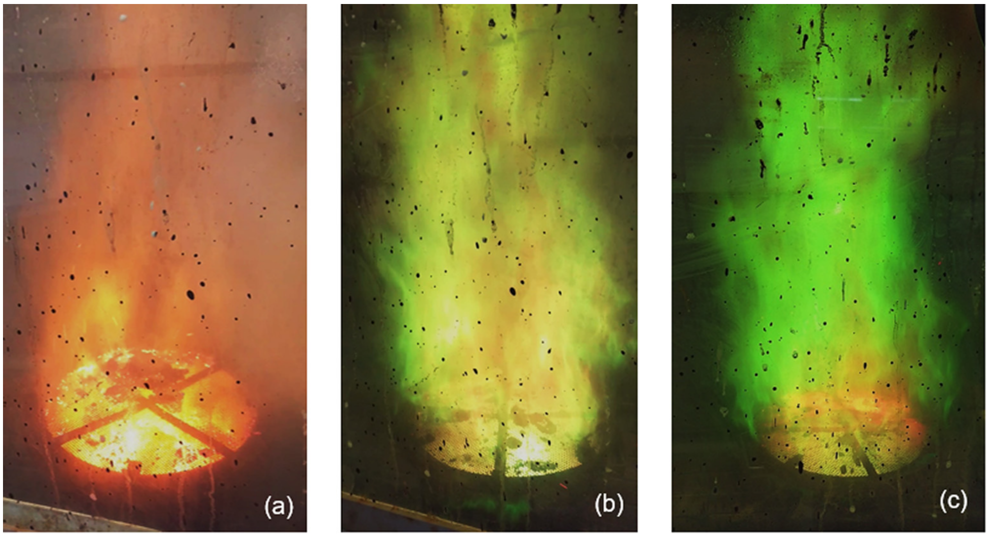

Fig. 2 Images of combustion flames captured during the syntheses of the ferrites: (a) NZ, (b) NZC2 and (c) NZC3.

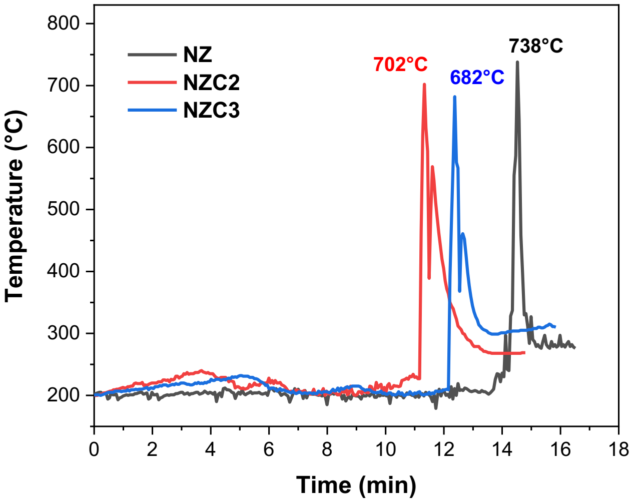

Fig. 3 Temperature versus time measured during the combustion syntheses of the ferrites.

$Ni_{0.25}Cu_{0.30}Zn_{0.45}Dy_xFe_{2\text{-}x}O_4$ (x = 0.0, 0.025, 0.05. 0.075 and 1.25) ferrite synthesized by sol–gel autocombustion route, they also confirmed the presence of hematite (Fe_2O_3) as segregated phase, in addition to the presence of the NiZnCu spinel ferrite as majoritary phase. However, although did not mention by the authors, but the diffractograms also showed small peaks characteristic of the segregated phase of ZnO, as observed at the present study.

It can be said that the appearance of these segregated phases is possibly related to the speed of the combustion reactions (total time less than 17 min), the short period of flames presence (18 to 24 s), and the low maximum temperature reached during the syntheses, which did not exceed 750 °C. However, even not allowing the formation or complete crystallization of the desired spinel phase, this does not compromise the efficiency of the combustion synthesis, but only indicates the need for changes in the synthesis conditions to obtain a single-phase product, if it is essentially necessary. In the present study, however, it was observed that by submitting these NiZnCu ferrites with presence of segregated phases to a sintering process at 1200 °C/1h, made it possible the monophasic formation of the cubic structure of $Ni_{0.5\text{-}x}Zn_{0.5\text{-}x}Cu_{2x}Fe_2O_4$ spinel ferrite, evidenced by the peaks correspondent to the (111), (220), (311), (222), (400), (422), (511) and (440) planes identified by the standard JCPDS file no. 48-0489, which showed themselves more intense and smaller basal width, characterizing a more crystalline material, as shown in Fig. 4b. Ergo, it can be said that the high temperature of sintering process provided the necessary energy for the metallic ions segregated at deleterious phases, to assume their position within the cubic structure of the inverse spinel, allowing the complete crystallization of the desired phase.

Hwang et al. (2005) and Dantas et al. (2020) when they studied the synthesis of NiZn ferrite by combustion reaction, varying the synthesis conditions, whether evaluating the excess or deficiency of fuel, or even the production scale, both attributed the presence of segregated phases to the low temperatures reached during syntheses, which did not exceed 800 °C.

Table 1 Parameters of temperature and time measured during the combustion syntheses of $Ni_{0.5\text{-}x}Zn_{0.5\text{-}x}Cu_{2x}Fe_2O_4$ (x = 0; 0.10 and 0.15) ferrites.

Sample	x (mol)	T_{max} (°C)	t_r (min)	t_f (s)	M (g)	Color (flame)
NZ	0	738	16.5	18	209	orange
NZC2	0.1	702	14.8	24	215	greenish-orange
NZC3	0.15	682	15.9	21	213	green

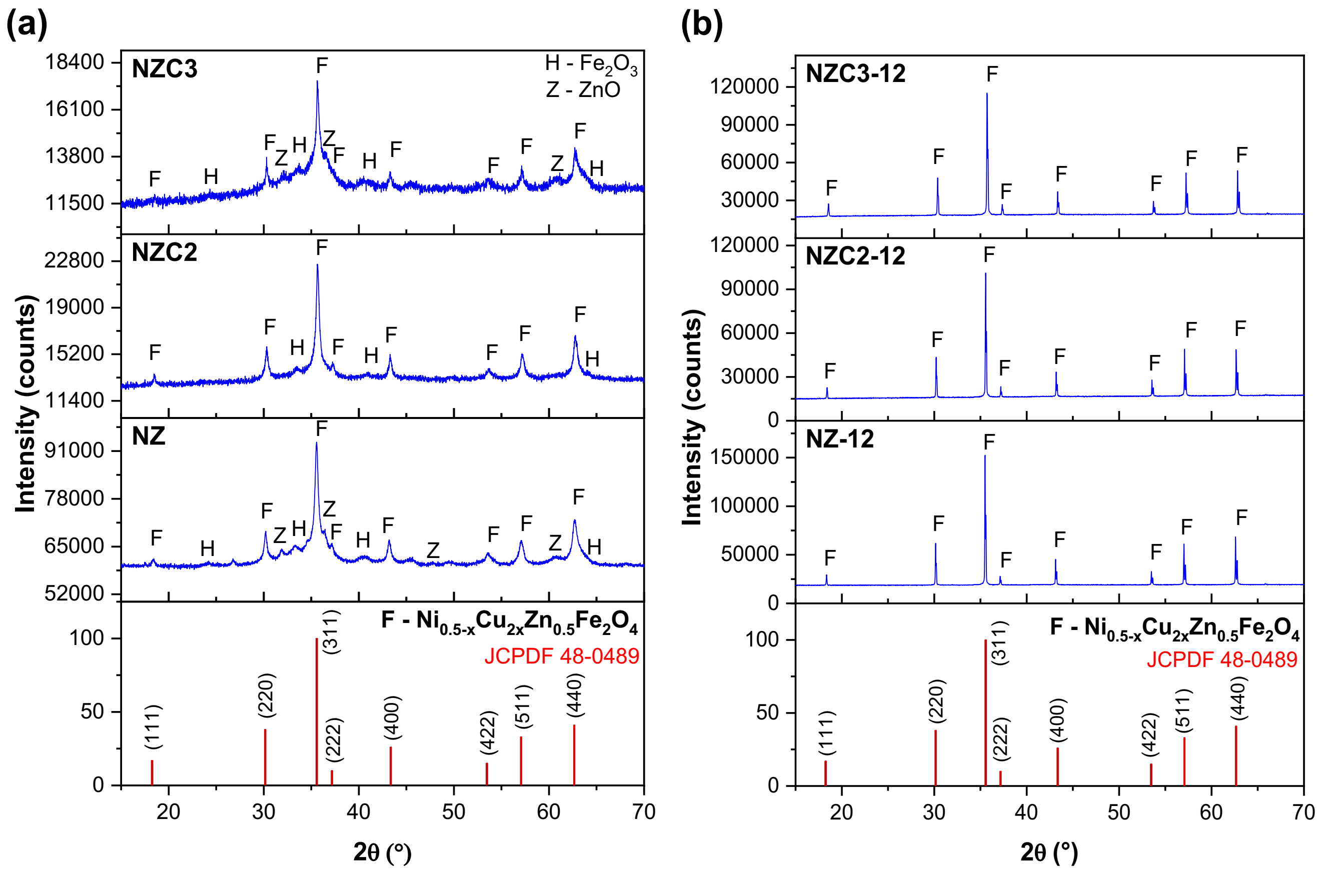

Fig. 4 X-ray diffraction curves of $Ni_{0.5\text{-}x}Zn_{0.5\text{-}x}Cu_{2x}Fe_2O_4$ (x = 0; 0.10 and 0.15): (a) as synthesized, and (b) sintered at 1200 °C/1 h.

Pozo López et al. (2010) studied the synthesis of NiZn ferrite by the solid state reaction method via ball milling, and only obtained the formation of the desired phase after 260 h of milling under atmospheric air, and even so, presenting hematite as secondary phase; and only under argon atmosphere, the authors obtained NiZn ferrite in its monophasic form. Peng et al. (2017) synthesized NiZn ferrite by the coprecipitation method, and managed to obtain the spinel ferrite after approximately a period of 6 h, involving a series of steps, and also presenting the hematite as secondary phase. In other words, comparing the combustion reaction with the methods described above, it can confirm even more the advantage of combustion synthesis at the production of a final product of simple way, since it does not involve multiple steps, and because it is efficiently fast, with duration of only some minutes. Furthermore, although the combustion reaction method is already a well-established technique when it comes to bench-scale production (Leal et al., 2018; Dantas et al., 2017; Mapossa et al., 2020; Hwang et al., 2005), the present study seeks to expand the use of the technique with pilot-scale production, that is, 200 g/batch of spinel-type ceramic phases, like the NiZnCu ferrite.

Table 2 lists the values of crystallite size (S_c), crystallinity (X_c), theoretical (a_{th}) and experimental (a_{exp}) lattice parameter, X-ray density (d_{XRD}), experimental density obtained by helium pycnometry (d_{EXP}), and relative density (d_{REL}) referring to the $Ni_{0.5\text{-}x}Zn_{0.5\text{-}x}Cu_{2x}Fe_2O_4$ (x = 0; 0.10 and 0.15) system as synthesized and sintered at 1200 °C/1 h.

In general, it can be said that the more copper was introduced in the $Ni_{0.5\text{-}x}Zn_{0.5\text{-}x}Cu_{2x}Fe_2O_4$ system, the smaller the crystallite size and the crystallinity of the formed ferrites, as shown in Fig. 5.

Among the as synthesized ferrites (NZ, NZC2 and NZC3), it was observed a slight decrease in crystallite size, whose values were 25.8, 25.5 and 24.9 nm, and also in crystallinity, with values of 60.3, 51.3 and 40.9%, respectively, which is possibly related to the energy supplied for the formation and growth of the crystals by the synthesis temperatures reached during combustion, whose values were 738 °C, 702 °C and 682 °C, respectively. That is, the higher the synthesis temperature, the greater the energy supplied for crystal growth, therefore, the larger the crystallite size and crystallinity of the sample. The same behavior, however, enhanced by the greater energy supplied during sintering (1200 °C/1 h), continued to be observed for ferrites NZ-12, NZC2-12 and NZC3-12, that is, the higher the Cu content introduced in the $Ni_{0.5\text{-}x}Zn_{0.5\text{-}}xCu_{2x}Fe_2O_4$ system, the crystallite size was smaller, with values ranging from 88.4 to 79.0 nm, and the crystallinity from 86.4 to 64.1%. Comparing the samples as synthesized with the sintered ones, increases of 241%, 243% and 217% were observed in the crystallite sizes, and 43%, 64% and 57% in the crystallinity values of the ferrites. Lv et al. (2016) when synthesized $Ni_{0.5}Zn_{0.5}Fe_2O_4$ ferrite by sol–gel method and evaluated the effect of calcination at temperatures of 600, 700, 800, 900 and 1000 °C over a period of 1 h, they observed a gradual increase in the crystallite size, whose values were 25.3, 37.2, 73.6, 95.4 and 112 nm, respec-

Table 2 Crystallite size (S_c), crystallinity (X_c), theoretical and experimental lattice parameter (a_{th}; a_{exp}), X-ray density (d_{XRD}), experimental density obtained by helium pycnometry (d_{EXP}) and relative density (d_{REL}) of $Ni_{0.5-x}Zn_{0.5-x}Cu_{2x}Fe_2O_4$ ferrites as synthesized and sintered at 1200 °C/1 h.

	Sample	S_c (nm)	X_c (%)	a_{th} (Å)	a_{exp} (Å)	d_{XRD} (g/cm^3)	d_{EXP} (g/cm^3)	d_{REL}
Synthesized	NZ	25.8	60.3	8.381	8.371	5.384	5.379	0.999
	NZC2	25.5	51.3	8.356	8.355	5.435	5.422	0.998
	NZC3	24.9	40.9	8.357	8.359	5.417	5.474	1.010
Sintered	NZ-12	88.4	86.4	8.381	8.385	5.357	5.397	1.007
	NZC2-12	87.6	84.1	8.356	8.374	5.385	5.476	1.017
	NZC3-12	79.0	64.1	8.357	8.337	5.460	5.563	1.019

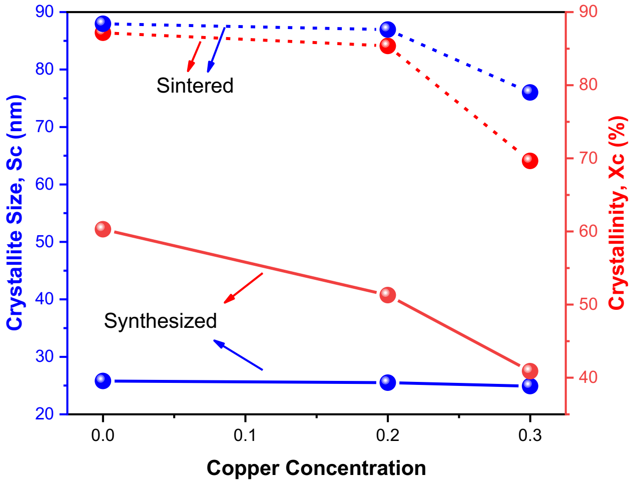

Fig. 5 Variation of crystallite size and crystallinity with the Cu^{2+} ions concentration at $Ni_{0.5-x}Zn_{0.5-x}Cu_{2x}Fe_2O_4$ ferrites as synthesized and sintered at 1200 °C/1 h.

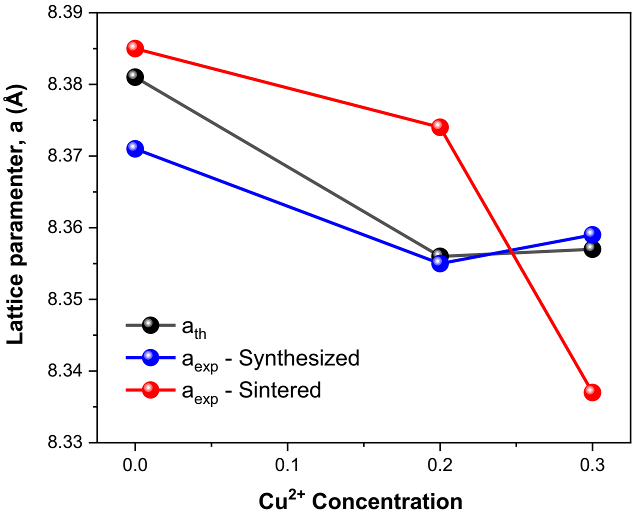

Fig. 6 Variation of the theoretical and experimental lattice parameter with the Cu^{2+} ions concentration at $Ni_{0.5-x}Zn_{0.5-x}Cu_{2x}Fe_2O_4$ ferrites as synthesized and sintered at 1200 °C/1h.

tively, confirming the contribution of temperature to crystal growth, similar to the behavior observed in the present study. The reduction in crystallite size and crystallinity with the addition of Cu has also been reported by Caltun et al. (2001), when they synthesized the NiZn ferrite doped with Cu via conventional ceramic method.

The variation of theoretical and experimental lattice parameter as a function of Cu^{2+} ions concentration in the $Ni_{0.5-x}Zn_{0.5-x}Cu_{2x}Fe_2O_4$ system as synthesized and after sintering at 1200 °C/1 h is shown in Fig. 6. Taking into account that the theoretical lattice parameters were calculated as a function of the Cu-doping in NiZn ferrite and the ionic radii sizes present in each system, whose adopted values were 0.69 Å (Ni^{2+}), 0.74 Å (Zn^{2+}), 0.73 Å (Cu^{2+}), 0.64 Å (Fe^{3+}) and 1.40 Å (O^{2-}), it was possible to notice a tendency of reduction of the lattice parameter of −0.30% and −0.29% when compared to the theoretical lattice parameter of $Ni_{0.5}Zn_{0.5}Fe_2O_4$ ferrite, whose value was 8281 Å, that is, there was a decrease followed by a subtle increase (+0.1%). Contrary to what is seen in the literature (Das and Singh, 2016; Houshiar and Jamilpanah, 2018; Ruiz et al., 2013; Dantas et al., 2017), where Cu^{2+} normally replaces Ni^{2+} in NiZn ferrite, and occurs a trend towards an increase in the lattice parameter, since the radius of Cu^{2+} (0.73 Å) is greater than that of Ni^{2+} (0.69 Å), in the present study, however, there is a partial and proportional replacement of the Ni^{2+} and Zn^{2+} ions by the Cu^{2+} ions, as represented by the $Ni_{0.5-x}Zn_{0.5-x}Cu_{2x}Fe_2O_4$ (for x = 0, 0.10 and 0.15) system, and that justifies the slight decrease in the lattice parameter, since Cu^{2+} ions are approximately 5.5% higher than Ni^{2+} and 1.4% lower than Zn^{2+}.

Following the same tendency of the theoretical lattice parameters, the experimental lattice parameters of the as synthesized ferrites (NZ, NZC2 and NZC3) showed decreases of −0.19% and −0.14% after doping with 0.2 and 0.3 mol of Cu, respectively, when compared with the $Ni_{0.5}Zn_{0.5}Fe_2O_4$ ferrite lattice parameter (8.271 Å), that is, after doping there was a decrease of −0.19 followed by an increase of +0.05%. Then, analyzing the lattice parameters of the sintered ferrites (NZ-12, NZC2-12 and NZC3-12), it was observed decreases of −0.13% and −0.57% after doping with 0.2 and 0.3 mol of Cu in the $Ni_{0.5-x}Zn_{0.5-x}Cu_{2x}Fe_2O_4$ system. In general, this proximity to the experimental and theoretical values demonstrates the success of the synthesis by combustion reaction for the ferrite systems under study.

Fig. 7 shows the variation of X-ray density and experimental density obtained by helium (He) pycnometry as a function of the Cu^{2+} ions concentration introduced into the $Ni_{0.5-x}Zn_{0.5-x}Cu_{2x}Fe_2O_4$ system as synthesized and sintered at 1200 °C/1 h.

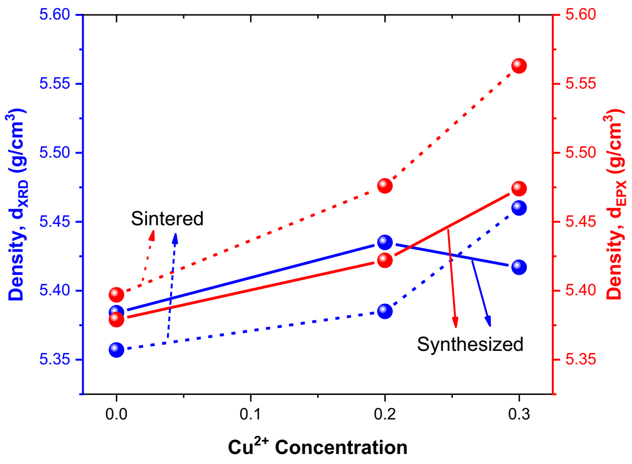

Fig. 7 Variation of X-ray and experimental density with the Cu^{2+} ions concentration at $Ni_{0.5\text{-}x}Zn_{0.5\text{-}x}Cu_{2x}Fe_2O_4$ ferrites as synthesized and sintered at 1200 °C/1 h.

In general, an increase in density is observed with the introduction of Cu in the $Ni_{0.5\text{-}x}Zn_{0.5\text{-}x}Cu_{2x}Fe_2O_4$ system, exception given to the as synthesized ferrite with 0.3 mol of Cu^{2+} (NZC3), which showed a reduction of 0.34% when compared to the ferrite with 0.2 mol of Cu^{2+} (NZC2). This behavior is justifiable, since the density is a measure inversely proportional to the lattice parameter (see Eq. (5)), as shown in Table 2 and Fig. 6, where NZC3 ferrite showed a slight increase in its lattice parameter compared to NZC2 ferrite. Ehi-Eromosele et al. (2015) when studied the fuel content in the synthesis by combustion reaction of the $Co_{0.8}Mg_{0.2}Fe_2O_4$ ferrite, they observed a similar behavior, because the lower the lattice parameter, the greater the X-ray density achieved. Mapossa et al. (2020) reported the synthesis of $Ni_{0.3}Zn_{0.7}Fe_2O_4$ ferrite by the combustion reaction method, with crystallite size of 20.0 nm, X-ray density of 5.330 g/cm^3, and experimental density of 5.334 g/cm^3. Bajorek et al. (2019) when they synthesized $Ni_{0.5}Zn_{0.5}Fe_2O_4$ ferrite by the co-precipitation method, they reported a crystallite size of 20.4 nm and X-ray density of 5.32 g/cm^3. The results reported by the authors showed density values very close to that of $Ni_{0.5}Zn_{0.5}Fe_2O_4$ ferrite under study, but smaller crystalline size.

Regarding the relative density (Table 2), it was observed values close to 1, indicating the good admeasurement between the X-ray densities and the absolute densities obtained by helium pycnometry.

3.3. Semi-quantitative oxides analysis

Table 3 shows the experimental and theoretical values of the semi-quantitative analysis of oxides, determined by EDX, referring to the $Ni_{0.5\text{-}x}$Zn0.5-x$Cu_{2x}Fe_2O_4$ ferrites as synthesized and sintered at 1200 °C/1 h. The results of the experimental values of the oxide composition are consistent with the calculated theoretical values, presenting percentage differences below 1.0%. This indicates that the expected stoichiometry based on the preparation of the $Ni_{0.5\text{-}x}$Zn0.5-x$Cu_{2x}Fe_2O_4$ cubic spinel ferrite was maintained in the samples synthesized by combustion reaction and after the sintering process. The samples NZC3, NZ12, NZC2-12 and NZC3-12 showed traces of impurities of the oxides Al_2O_3 and/or SiO_2, which are possibly associated with the beneficiation process, which made use of the porcelain mortar; and with the contact sample/ceramic plate during the sintering process.

3.4. Textural characterization

Fig. 8 shows the N_2 adsorption/desorption isotherms referring to the textural characterization of $Ni_{0.5\text{-}x}Zn_{0.5\text{-}x}Cu_{2x}Fe_2O_4$ ferrites as synthesized and sintered at 1200 °C/1 h. It is possible to observe that the as synthesized ferrites (Fig. 8a) indicate type IV isotherms, typical of mesoporous materials, according to the IUPAC classification (Sing et al., 1985). And the sintered ferrites (Fig. 8b) indicate isotherms tending to type II mixed with type IV, since they present a slight delay in the desorption process (Sing et al., 1985). Type II isotherm is characteristic of non-porous or macroporous materials, while type IV isotherm, as already mentioned, is typical of mesoporous materials. All isotherms present a slight inflection around relative pressure of approximately 0.2, indicating the monolayers adsorption on the surface of the material, including the surfaces of the micropores and mesopores. Between 0.25 and 0.50 P/P_0, intermediate relative pressures, there is a linear increase of the adsorbed volume that can be attributed to the capillary condensation phenomenon in the mesopores. Then, at relative pressures above 0.50, the increase in the adsorbed volume under higher relative pressures is associated with the multilayer adsorption and/or to the condensation in the secondary mesopores. And finally, at relative pressures above 0.80, the adsorbed volume may be associated to the filling of the voids between the particles that can be considered as porosity (Oliveira and Andrada, 2019). All of these transitions are much more well-defined in the isotherms of the as synthesized ferrites (Fig. 8a), since they present well-defined hysteresis loops, which may be attributed to the capillary condensation, that occurs because of the delay in pore condensation.

Also according to the IUPAC classification (Sing et al., 1985), the as synthesized ferrites (Fig. 8a) present hysteresis loop of type H2, indicating the possible presence of cylindrical pores, open and closed with necking, resulting in an irregular morphology with a bottle aspect. However, the sintered ferrites (Fig. 8b) presented hysteresis loop of type H3, where the pores have a wedge or slit geometry, resulting from agglomerates of parallel plates-shaped particles. These considerations corroborate the results obtained in the morphological analysis for the under study ferrites, as shown in Figs. 9 and 10.

Table 4 shows the results of textural parameters obtained from the N_2 adsorption/desorption isothermal data for the $Ni_{0.5\text{-}x}Zn_{0.5\text{-}x}Cu_{2x}Fe_2O_4$ (x = 0; 0.10 and 0.15) ferrites as synthesized and sintered at 1200 °C/1 h. In general, whether in ferrites as synthesized or sintered, it is observed that the introduction and increase of Cu^{2+} content in the $Ni_{0.5\text{-}x}Zn_{0.5\text{-}x}Cu_{2x}Fe_2O_4$ system led to an increase in the particle size, whose values ranged from 25.93 to 28.21 nm and from 190.01 to 376.20 nm, and consequently, a reduction in the surface area, whose values ranged from 38.851 to 43.013 m^2/g and from 2.867 to 5.851 m^2/g, respectively. As expected, the most significant changes were observed when comparing the textural parameters of ferrites before and after sintering, since the energy supplied during sintering was much greater than in the synthesis process. Therefore, it was observed percentage

Table 3 Percentages of theoretical and experimental oxides determined by EDX of $Ni_{0.5-x}Zn_{0.5-x}Cu_{2x}Fe_2O_4$ ferrites as synthesized and sintered at 1200 °C/1 h.

Samples		Oxides (%)				
		NiO	ZnO	CuO	Fe_2O_3	Outros*
Synthesized	**NZ**	E – 16.117 T – 15.696 D – 0.421	E – 16.468 T – 17.108 D – −0.640	–	E – 67.415 T – 67.196 D – 0.219	–
	NZC2	E – 12.874 T – 12.541 D – 0.333	E – 13.098 T – 13.669 D – −0.571	E – 6.108 T – 6.678 D – −0.570	E – 67.920 T – 67.112 D – 0.808	–
	NZC3	E – 11.212 T – 10.966 D – 0.246	E – 11.694 T – 11.953 D – 0.259	E – 9.121 T – 10.011 D – −0.890	E – 67.756 T – 67.070 D – 0.686	E – 0.217[a]
Sintered	**NZ-12**	E – 15.462 T – 15.696 D – −0.234	E – 16.359 T – 17.108 D – −0.749	–	E – 68.024 T – 67.196 D – 0.828	E – 0.155[b]
	NZC2-12	E – 12.414 T – 12.541 D – −0.127	E – 13.261 T – 13.669 D – −0.408	E – 6.097 T – 6.678 D – −0.581	E – 67.889 T – 67.112 D – 0.777	E – 0.339[c]
	NZC3-12	E – 11.459 T – 10.966 D – 0.493	E – 11.576 T – 11.953 D – −0.377	E – 9.173 T – 10.011 D – −0.838	E – 67.662 T – 67.070 D – 0.592	E – 0.130[d]

Note: T - theoretical value calculated by Eq. (7); E - experimental value; and D - difference between the experimental and theoretical values. * Impurities: [a] Al_2O_3 (0.217%); [b] SiO_2 (0.155%); [c] Al_2O_3 (0.202%) and SiO_2 (0.137%); [d] SiO_2 (0.130%).

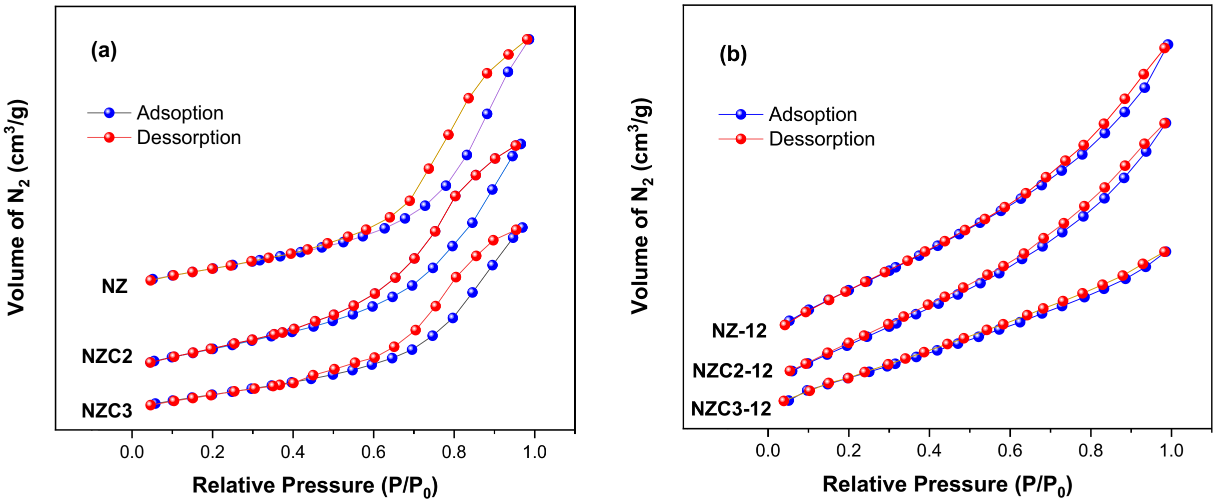

Fig. 8 N_2 adsorption/desorption isotherms for $Ni_{0.5-x}Zn_{0.5-x}Cu_{2x}Fe_2O_4$ ferrites: (a) as synthesized and (b) sintered at 1200 °C/1h.

increases in particle size of 633%, 1229% and 1233% for the ferrites NZ-12, NZC2-12 and NZC3-12, respectively, when compared with the non-sintered ones. This increase in particle size can be attributed to the acceleration of the interdifusion process of the cations promoted by Cu^{2+} ions (Rezlescu et al., 2000; Dimri et al., 2006), and to the increased reactivity of ferrite fine particles that possibly coalesce to form larger particles, especially after the sintering process, which leads to a reduction of pores and contraction of volume, thus contributing to greater density. It was observed pore radii ranging from 21.189 to 22.637 Å and from 16.691 to 16.797 Å, and pore volume ranging from 0.118 to 0.175 cm^3/g and from 0.006 to 0.011 cm^3/g, for the ferrites as synthesized and sintered, respectively. That is, after sintering, the ferrites NZ-12, NZC2-12 and NZC3-12 showed reductions of 93.7%, 94.7% and 94.5% in the pore volume, and of 25.8%, 23.7% and 20.9% in the pore radius.

Furthermore, taking into account that the addition of Cu^{2+} due to its atomic mobility favors the decrease of the sintering temperature of the system (Rezlescu et al., 2000; Nakamura and Okano, 1997), it can be said that Cu accelerates the whole process of pore elimination, and growth and coalescence of nanoparticles. Analyzing the NZ-12, NZC2-12 and NZC3-12 ferrites, it is observed that the introduction of 0.2 and 0.3 mol of Cu in the NiZn ferrite led to significant increases in particle size, with additions of 86.07% and 97.99% when compared to the undoped NiZn ferrite (NZ-12), and decreases of 36.4% and 45.4% in the pore volume,

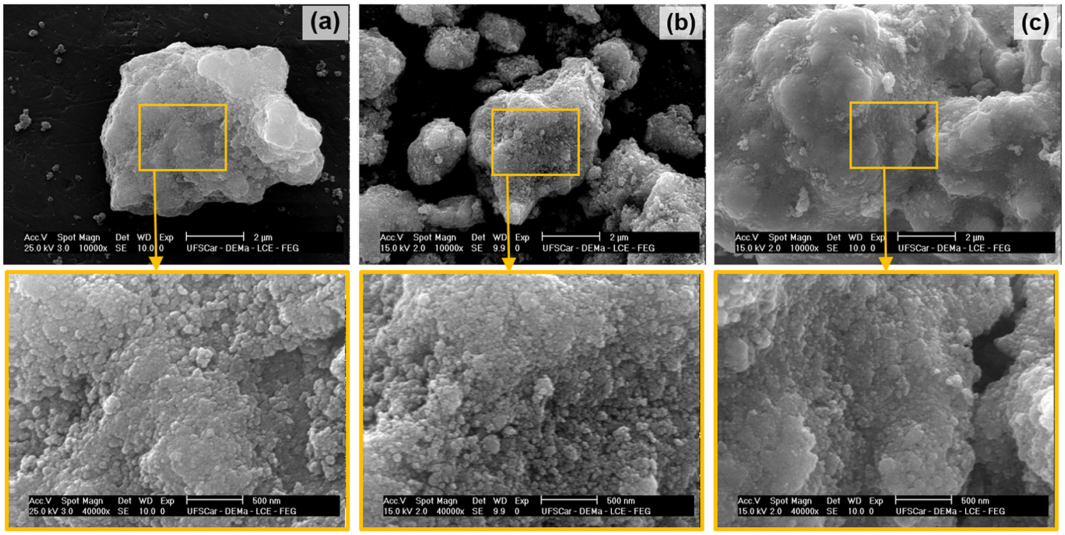

Fig. 9 SEM of the as synthesized ferrites: (a) NZ, (b) NZC2 and (c) NZC3, with increase of 10.000× and zoom of 40.000×.

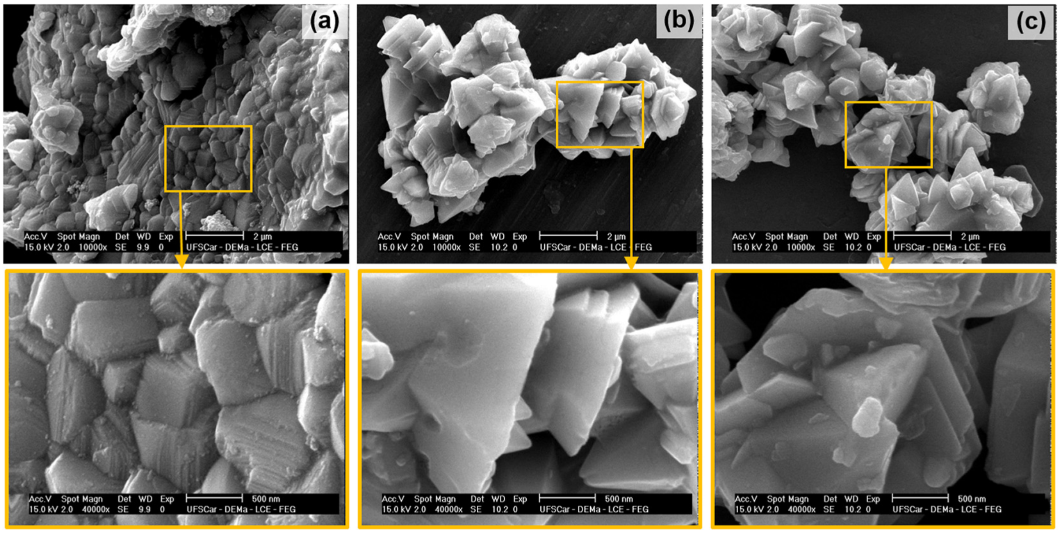

Fig. 10 SEM of the ferrites sintered at 1200 °C/1 h: (a) NZ-12, (b) NZC2-12 and (c) NZC3-12, with increase of 10.000× and zoom of 40.000×.

Table 4 Specific surface area (S_{BET}), particle size (D_{BET}), pore volume (V_P), pore radius (R_P) and the particle size/crystallite size ratio (D_{BET}/S_C) of $Ni_{0.5-x}Zn_{0.5-x}Cu_{2x}Fe_2O_4$ ferrites as synthesized and sintered at 1200 °C/1h.

	Sample	S_{BET} (m^2/g)	D_{BET} (nm)	V_P (cm^3/g)	R_P (Å)	D_{BET}/S_C*
Synthesized	NZ	43.013	25.93	0.175	22.637	1.005
	NZC2	41.597	26.60	0.132	21.891	1.043
	NZC3	38.851	28.21	0.118	21.189	1.133
Sintered	NZ-12	5.851	190.01	0.011	16.797	2.149
	NZC2-12	3.099	353.56	0.007	16.691	4.036
	NZC3-12	2.867	376.20	0.006	16.764	4.762

* S_C = Crystallite size from XRD data.

respectively. As for the values of the particle size/crystallite size ratio (D_{BET}/S_C), it is noticed that as Cu ions were introduced in NiZn ferrite, the value of this ratio increased, as well as its significant increase after sintering, whose values doubled or quadrupled. This indicates a more polycrystalline characteristic of the ferrites after sintering, since one particle is constituted by greater number of crystals (Dantas et al., 2017).

3.5. Morphological characterization

Figs. 9 and 10 show the scanning electron micrographs for the $Ni_{0.5-x}Zn_{0.5-x}Cu_{2x}Fe_2O_4$ (x = 0; 0.10 and 0.15) ferrites as synthesized and sintered at 1200 °C/1h, respectively. According to the micrographs of Fig. 9, referring to the as synthesized ferrites, it is observed agglomerates formed by nanoparticles joined by weak forces, with irregular shapes and sizes, and with a great presence of interparticle porosity, characteristic of powders synthesized by combustion reaction, in response to the great evolution of gases generated during the reactions. As combustion syntheses occur in abrupt and quick way, the nucleation mechanism overlaps growth mechanism of the particles, forming powders with nanometric characteristic. Leal et al. (2018) when synthesize MFe_2O_4 (M = Cu, Ni, Co, Mn and Fe) spinel ferrites by combustion reaction, they also observed morphologies formed by agglomerates of weakly bound particles, with friable aspect, attributing this characteristic to the synthesis method.

Analyzing the SEM images of the sintered ferrites, a great change in the morphology of the formed ferrites is observed. At first, the grain growth is observed in response to the energy supplied during the sintering process. The sintered sample of the undoped $Ni_{0.5}Zn_{0.5}Fe_2O_4$ ferrite, NZ-12 (Fig. 10a), shows a morphology with wide grain size distribution, with values ranging from 0.22 to 1.65 μm, with irregular shapes, and constituted of thin plates piled in parallel. After the Cu addition in the $Ni_{0.5}Zn_{0.5}Fe_2O_4$ system, the change in ferrite morphology is notable, where the grains are no longer made up of slim and irregular plates, assuming defined and varied polygonal shapes, such as hexagons and pyramids, also with a wide size distribution, ranging from 0.52 to 2.15 μm and 0.54–1.90 μm, and average sizes of 1.31 and 1.33 μm, for the ferrites doped with 0.2 and 0.3 mol of Cu (NZC2-12 and NZC3-12), respectively. This wide distribution in grain size is result of the large amount of nucleation and growth of nanocrystallites. The growth mechanism can be explained as an oriented aggregation of primary nanoparticles, involving the self-assembly of adjacent nanoparticles in a common crystallographic orientation and joined to form planar interfaces, minimizing the overall energy of the system (Liu et al., 2009).

This change in shape and morphology with the Cu addition, possibly is correlated with the dimensions of the ionic radii of the precursors. During the synthesis by combustion reaction, which in turn are fast reactions, the precursors are adsorbed onto the preferred planes in short intervals of time, changing the growth kinetics at nucleation stage. Therefore, after sintering, the Cu ions, which have a high rate of interdiffusion in solid solution (Rezlescu et al., 2000), change the grain growth kinetics, modifying the collective behavior of van der Waals forces and electrostatic interactions that lead to the self-aggregation of nanoparticles in a specific direction (such as nanoplates), changing the morphology to better defined polygonal shapes, with greater thickness and apparently more dense, corroborating the results of density and textural analysis.

Das and Singh (2016), when evaluating the Cu-doping in NiZn ferrite, they observed changes in the shape and morphology of the particles, since the undoped NiZn ferrite presented particles with nanoplates format, as showed at the present study, and that after the Cu addition, it was observed a nanorods morphology, with growth directed towards a determined crystal axis. The authors also attributed this change in shape to the preferential growth kinetics of nanoparticles caused by copper.

3.6. Magnetic characterization

The magnetic study was carried out in order to investigate whether the Cu doping and the structural transitions after the sintering process generated effects on the magnetic properties of $Ni_{0.5-x}Zn_{0.5-x}Cu_{2x}Fe_2O_4$ (x = 0; 0.10 and 0.15) ferrites. The magnetic hysteresis loops (M × H) measured at room temperature with an applied field of 15 KOe are shown in Fig. 11, and illustrate the magnetic behavior of NiZnCu ferrites. It was observed that all ferrite systems presented narrow and well-defined S-shaped hysteresis loops, with low remaining magnetization (M_R) and coercivity (H_C) values, indicating a ferrimagnetic behavior typical of soft magnetic materials, i.e., which magnetize and demagnetize more easily (Sugimoto, 1999; Tsay et al., 2000; Dantas et al., 2017).

Table 5 reports the values of the magnetic parameters determined from hysteresis loops M × H, such as saturation magnetization (M_S), remnant magnetization (M_R), coercivity (H_C), remanence ratio (M_R/M_S) and Bohr magneton number (n_B) of the $Ni_{0.5-x}Zn_{0.5-x}Cu_{2x}Fe_2O_4$ ferrites as synthesized and sintered at 1200 °C/1 h.

The magnetic properties in nanoparticles are influenced by both intrinsic factors (chemical composition, cation preferential occupation and exchange interaction effect) and extrinsic factors (microstructure, porosity and grain size), which, in turn, are related to the synthesis and sintering processes (Dimri et al., 2006; Ahmed et al., 2004; Lima et al., 2008; Pozo López et al., 2010). In soft magnetic ferrites, the saturation magnetization directly depends on the net magnetization of the spinel lattice, which can be explained by the interaction between the magnetic moments of the two sublattices A and B, relative to the octahedral-site (B-type) and tetrahedral-site (A-type), according to the expression $M = M_B\text{-}M_A$ (Hajarpour et al., 2014; Bajorek et al., 2019; Houshiar and Jamilpanah, 2018). It is known that Ni^{2+} ions (2 μB) prefer to occupy octahedral sites, Zn^{2+} ions (0 μB) prefer tetrahedral sites, and Fe^{3+} (5 μB) and Cu^{2+} (1 μB) ions can occupy both the tetrahedral and octahedral sites, maintaining the preference for octahedral sites (B-type). Since the NiZn ferrite has twelve Fe^{3+} ions ($3d^64s^2$) and four Ni^{2+} ions ($3d^84s^2$) at octahedral positions, and inversely positioned, it has four Fe^{3+} ions and four Zn^{2+} ions ($3d^{10}4s^2$) at tetrahedral positions, which leads to a general cation distribution formula equivalent to $(Zn^{2+}_{0.5}Fe^{3+}_{0.5})^A[Ni^{2+}_{0.5}Fe^{3+}_{1.5}]^BO_4$. Therefore, the four Fe^{3+} ions at tetrahedral sites (A) are cancelled by the four Fe^{3+} ions at octahedral sites (B), remaining still eight Fe^{3+} ions at the octahedral sites (B).

With the Cu^{2+} doping into the NiZn ferrite, the Cu^{2+} ions ($3d^{10}4s^1$) partially replace the four Ni^{2+} ions at octahedral positions (B) and the four Zn^{2+} ions at the inverse tetrahedral positions (A). Taking into account the replacement of Ni^{2+} ions by Cu^{2+} ions at the B sites, the M_S value should initially decrease, since the magnetic moment of Cu^{2+} ions (1 μB) is lower than Ni^{2+} ions (2 μB).

Now, considering the partial replacement of Zn^{2+} ions by Cu^{2+} ions at A sites, and that the magnetic moment of

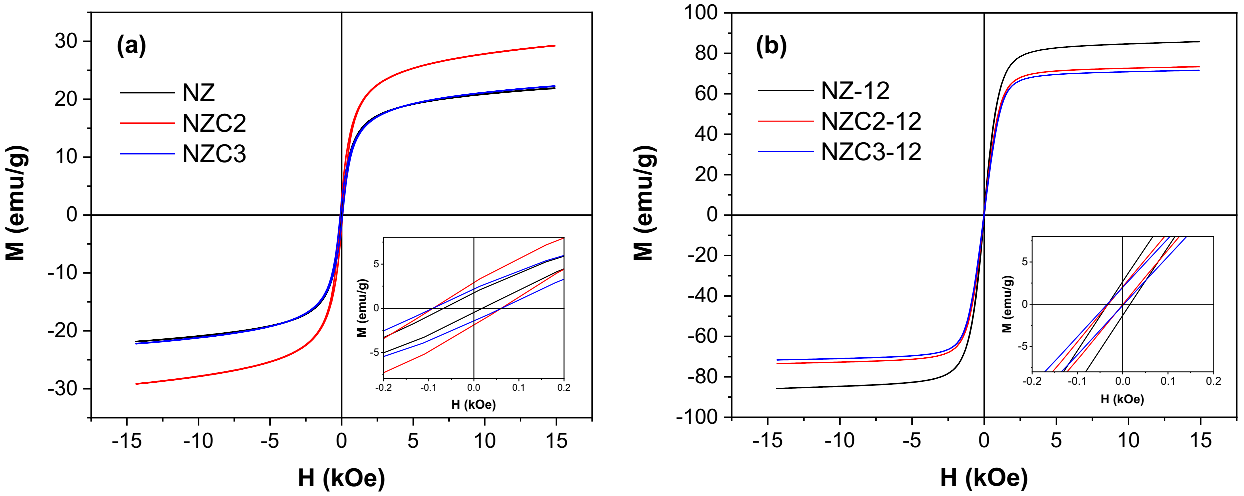

Fig. 11 Magnetic hysteresis loops of $Ni_{0.5\text{-}x}Zn_{0.5\text{-}x}Cu_{2x}Fe_2O_4$ (x = 0; 0.1 and 0.15 mol of Cu) ferrites: (a) as synthesized, and (b) sintered at 1200 °C/1 h.

Table 5 Saturation magnetization (M_S), remnant magnetization (M_R), coercivity (H_C), remanence ratio (M_R/M_S) and Bohr magneton number (n_B) of $Ni_{0.5\text{-}x}Zn_{0.5\text{-}x}Cu_{2x}Fe_2O_4$ (x = 0; 0.1 and 0.15) ferrites as synthesized and sintered at 1200 °C/1 h.

	Sample	M_S (emu/g)	M_R (emu/g)	H_C (Oe)	M_R/M_S	n_B
Synthesized	NZ	21.89	1.73	19.56	0.079	0.93
	NZC2	29.24	2.89	61.43	0.099	1.25
	NZC3	22.23	2.16	61.71	0.097	0.95
Sintered	NZ-12	85.80	2.67	16.42	0.031	3.65
	NZC2-12	73.28	2.07	1.02	0.028	3.12
	NZC3-12	71.57	2.01	2.75	0.028	3.05

Cu^{2+} ions (1 μB) is greater than Zn^{2+} ions (0 μB), one should also expect a reduction at M_S value, since the general magnetic moment balance (M_B-M_A) will also tend to decrease. However, as a consequence of Cu doping in NiZn ferrite, a reduction in the M_S value must be expected (Houshiar and Jamilpanah, 2018; Dantas et al., 2017; Das and Singh, 2016), and it was what really happened among the sintered $Ni_{0.5\text{-}x}Zn_{0.5\text{-}x}Cu_{2x}Fe_2O_4$ (x = 0; 0.10 and 0.15) ferrites, since as the contents of 0.2 and 0.3 mol of Cu were added, the lower was the M_S, whose values were 85.80, 73.28 and 71.57 emu/g for the NZ-12, NZC2-12 and NZC3-12 ferrites, respectively, as shown in Table 5 and Fig. 12. The same behavior was not observed among the as synthesized $Ni_{0.5\text{-}x}Zn_{0.5\text{-}x}Cu_{2x}Fe_2O_4$ ferrites, since the greater M_S value belonged to NiZn ferrite doped with 0.2 mol of Cu (NZC2), whose value was 29.24 emu/g, while the undoped NiZn ferrite (NZ) and the one doped with 0.3 mol of Cu (NZC3) showed values of 21.89 and 22.23 emu/g, respectively. This fact is possibly related to the greater segregation of the hematite (Fe_2O_3) and zinc oxide (ZnO) phases in NZ and NZC3 ferrites, as seen in the X-ray diffraction results (Fig. 4). Therefore, the exchange interaction between the segregated phases of Fe_2O_3 (antiferromagnetic or weak ferromagnetic) and ZnO (paramagnetic), together with the majoritary phase of the NiZnCu ferrite (ferrimagnetic), leads to a reduction in the total magnetic moment, accounting for losses at the magnetic properties of the material as a whole.

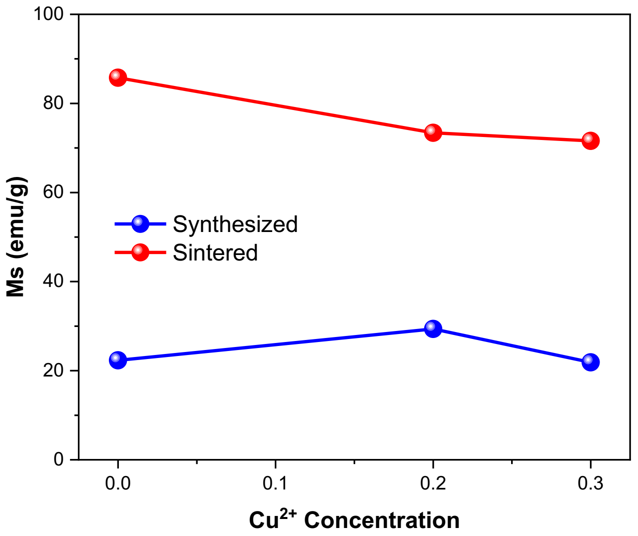

Fig. 12 Saturation magnetization (M_S) in function of the Cu^{2+} ions concentration at $Ni_{0.5\text{-}x}Zn_{0.5\text{-}x}Cu_{2x}Fe_2O_4$ ferrites as synthesized and sintered at 1200 °C/1 h.

Similar behavior of magnetic interference by segregated phases has been reported in the literature (Lv et al., 2016; Lima et al., 2008; Pereira et al., 1999; Pozo López et al., 2010). On the other hand, it is remarkable that part of the Zn^{2+} and Fe^{3+} ions that left the desired stoichiometric composition ($Ni_{0.5\text{-}x}Zn_{0.5\text{-}x}Cu_{2x}Fe_2O_4$) at the form of the Fe_2O_3

and ZnO segregated phases, led to the formation of ferrites with compositions with a greater relative quantity of Ni^{2+} and Cu^{2+} ions. That is, in the NZ ferrite case, the decrease in Zn^{2+} ions at A sites led to a greater occupation of Fe^{3+} ions at these sites, thus causing a reduction in the net magnetic moment of the spinel lattice (M_B-M_A). The same may have happened for the NZC3 ferrite, where Cu^{2+} and Fe^{3+} ions may have assumed the free positions left by the deficiency of Zn^{2+} ions in the tetrahedral sites (A).

Comparing the as synthesized ferrites with the sintered ones (Fig. 12), it was observed significant percentage increases of 292%, 151% and 222% in the M_S values of the NZ-12, ZNC2-12 and NZC3-12 sintered ferrites, respectively. It was also observed respective percentage reductions of 16%, 98% and 95% in the coercivity of the ferrites after sintering.

This increase in the M_S value and the reduction in the H_C value can be attributed to the increase in the particle size after sintering, which created regions of multidomains, and contributed to a greater number of domain walls. Knowing that the magnetization/demagnetization caused by domain wall motion requires less energy than that required by the single domain rotation; larger particles or grains, which have a greater number of walls, contribute more easily to the magnetization or demagnetization of the ferrite to detriment of possible rotations of monodomains (Costa et al., 2003; Yan et al., 2004; Lv et al., 2016; Liu et al., 2017c). So, the larger the particle size, the lower the coercivity. As reported in the literature (Ruiz et al., 2013; Houshiar and Jamilpanah, 2018; Caltun et al., 2001) and previously in this study, the increase in Cu concentration into the NiZn ferrite favors the increase in particle size, leading to the origin of multidomains, and consequently to lower values of coercivity. This behavior was observed for the sintered $Ni_{0.5\text{-}x}Zn_{0.5\text{-}x}Cu_{2x}Fe_2O_4$ ($x = 0$; 0.10 and 0.15) ferrites, since the magnetic properties of the as synthesized ferrites suffered interference from the presence of segregated phases.

All the ferrites showed low remnant magnetization (M_R), with values ranging from 1.73 to 2.89 emu/g, and remanence ratio (M_R/M_S) from 0.028 to 0.099. When the ratio M_R/M_S, also called squareness ratio, presents values around ~0.5 is indicative of small single-domain, with randomly oriented assembly of small particles. The lower values, as observed in the present study, are usually associated with larger particles and domain-wall formation (Praveena et al., 2015). These low values is also associated to characteristic of soft magnetic materials, which easily magnetizes and demagnetizes, presenting low residual magnetism (M_R) after removal of the magnetic field, that is, that needs some more time to relaxes to zero filed value. And values of M_R/M_S very close to 0 (zero) is associated of the superparamagnetic regime of ferrites (Kumar et al., 2014).

Since the Bohr magneton number (n_B) is a measure that is directly related to the saturation magnetization (M_S), then the greater the M_S value, the greater the n_B value. Therefore, the highest n_B values were achieved for the sintered ferrites, whose values ranged from 3.05 to 3.65, while the as synthesized ferrites showed values from 0.93 to 1.25.

Qinghui et al. (2012) studied the effect of sintering at temperatures ranging from 820 to 970 °C over the magnetic behavior of NiZnCu ferrites, and they observed M_S values between 21 and 30 emu/g. Nam et al. (2003) synthesized the NiZnCu ferrite by sol–gel method, and they observed a M_S value of 19 emu/g at room temperature. Pozo López et al. (2010) synthesized the NiZn ferrite by the ball milling method, they evaluated the grinding time and the sintering process at 1000 °C/1 h, and observed M_S values ranging from 1 to 30 emu/g. Dantas et al. (2020) reported M_S values ranging from 20 to 37 emu/g for the NiZn ferrite obtained by combustion reaction method. Therefore, it can be said that the M_S values achieved in the present study are in agreement with those reported by other authors, confirming the efficiency of the pilot-scale combustion synthesis of the NiZnCu ferrites under study.

3.7. Electromagnetic characterization

Fig. 13 shows the complex permittivity and permeability of $Ni_{0.5\text{-}x}Zn_{0.5\text{-}x}Cu_{2x}Fe_2O_4$ ($x = 0$; 0.10 and 0.15) ferrites as synthesized and sintered at 1200 °C/1h in the frequency range of 8.2 to 12.4 GHz (X-band). It can be seen that the sintered ferrites showed the highest values of complex permittivity and permeability when compared with the non-sintered ferrites. It is also noted that the introduction of Cu^{2+} in NiZn ferrite contributed to a reduction in the real permittivity and permeability values (ε', μ'). According to Fig. 13a, real permittivity (ε') increased slightly with increasing frequency in all samples, with values ranging from 3.9 to 4.7. All the ferrites exhibited very low and almost constant imaginary permittivity values (ε'') throughout the frequency range. Analyzing Fig. 13b, it is observed that real and imaginary permeability (μ', μ'') decrease with increasing frequency. The real permeability values (μ') ranged from 0.83 to 1.03. The NZC3-12 ferrite was responsible for the highest value of imaginary permeability (μ'') throughout the X-band, reaching a maximum value of 0.19 at 8.2 GHz and a minimum value of 0.06 at 12.4 GHz. Therefore, it can be said that the greatest contribution to electromagnetic loss is due to magnetic loss.

Figs. 14, 15 and 16 show the calculated reflection loss (R_L) as a function of the composition, material's thickness, and frequency in the 8.2–12.4 GHz range for all $Ni_{0.5\text{-}x}Zn_{0.5\text{-}x}Cu_{2x}Fe_2O_4$ ($x = 0$; 0.10 and 0.15) ferrites as synthesized and sintered at 1200 °C/1 h. In general, it is observed that the behavior of the electromagnetic properties of $Ni_{0.5\text{-}x}Zn_{0.5\text{-}x}Cu_{2x}Fe_2O_4$ ferrites is influenced by both the Cu doping as well as the sintering heat treatment. Among the as synthesized ferrites, the greatest reflectivity was shown by NZC2 ferrite (Fig. 15a), with a narrow and V-shaped absorption profile, and R_L of −2.5 dB, corresponding to 42% attenuation in the region of 11.5 GHz for the thickness of 4 mm. NZC3 ferrite (Fig. 16a) also showed a narrow and V-shaped absorption profile, but with a lower R_L value, around −1 dB (17%) at 11 GHz frequency, also referring to the 4 mm thickness. Along the other frequencies at the X-band, these NZC2 and NZC3 ferrites showed R_L values ranging from approximately −0.4 to −1 dB and −0.4 to −0.8 dB, respectively. For NZ ferrite (Fig. 14a), it was observed R_L values ranging from −0.8 to −1.4 dB over the entire X-band, with the greatest attenuation for the thickness of 4 and 4.5 mm.

Among the ferrites sintered at 1200 °C/1h, it is observed that the NZ-12 and NZC2-12 ferrites have similar absorption profiles, that is, the highest absorptions occurred at low frequencies, around 8.2 GHz, tending to saturate at lower frequencies, below the X-band, and decreasing as the frequency was increasing until 12.4 GHz. NZ-12 ferrite showed R_L of

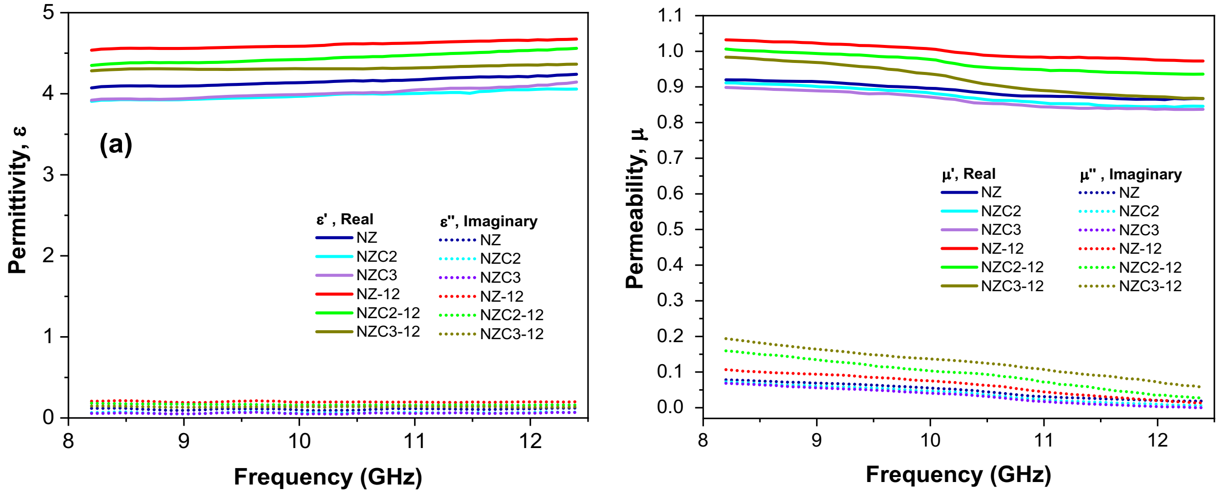

Fig. 13 Complex permittivity (a) and permeability (b) of $Ni_{0.5-x}Zn_{0.5-x}Cu_{2x}Fe_2O_4$ (x = 0; 0.10 and 0.15) ferrites as synthesized and sintered at 1200 °C/1 h.

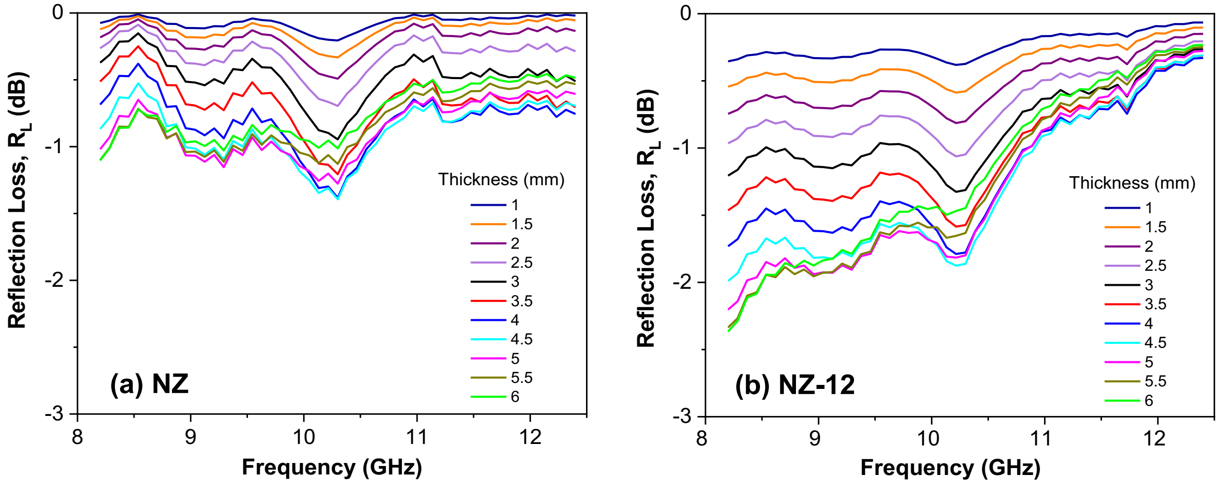

Fig. 14 Reflection loss (R_L) curves versus frequency of the samples: (a) NZ and (b) NZ-12.

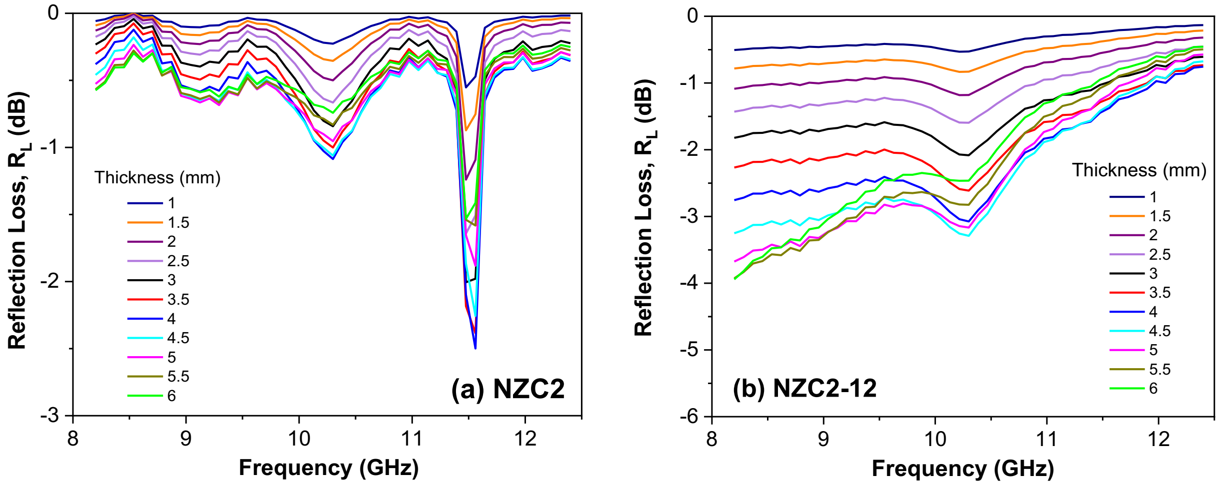

Fig. 15 Reflection loss (R_L) curves versus frequency of the samples: (a) NZC2 and (b) NZC2-12.

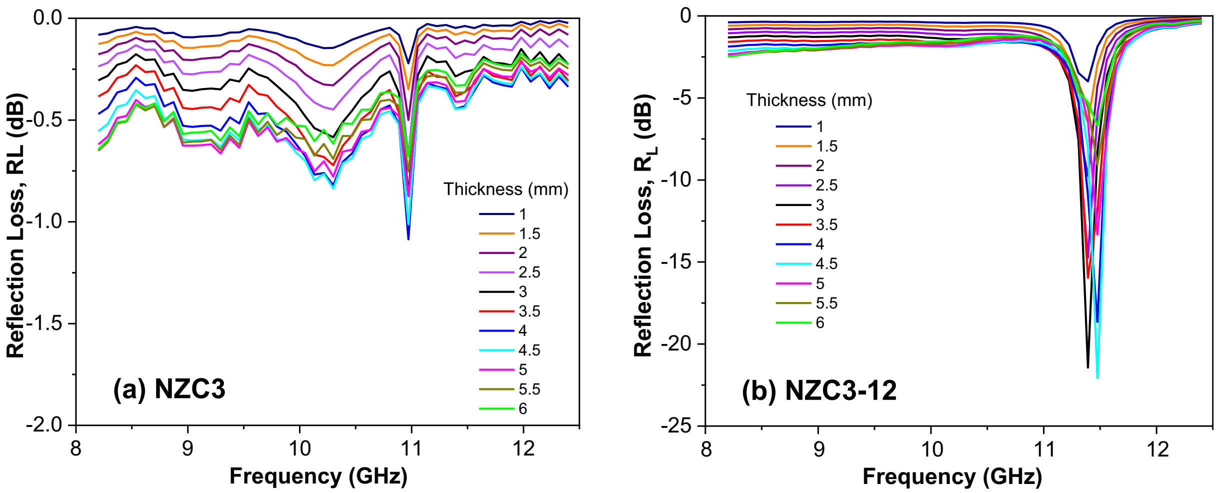

Fig. 16 Reflection loss (R_L) curves versus frequency of the samples: (a) NZC3 and (b) NZC3-12.

−2.3 dB at 8.2 GHz, equivalent to an approximately 38% attenuation for the thicknesses of 5.5 and 6 mm, and R_L of −1.8 dB (30%) at 10.3 GHz for the thicknesses of 4.5 and 5 mm. NZC2-12 ferrite showed R_L values close to −4 dB at 8.2 GHz, corresponding to approximately 72% attenuations for thicknesses of 5 to 6 mm, and R_L of approximately −3.3 dB (69%) at 10.3 GHz for the thicknesses of 4.5 and 5 mm. In NZC3-12 ferrite, however, the absorption profile changes significantly, with the appearance of an intense V-shaped peak, with R_L value of −22.2 dB, corresponding to an approximately 99.8% attenuation in the region of 11.5 GHz, for the 4.5 mm thickness, thus guaranteeing its potential for RAM application. Some studies confirm the improvement of the electromagnetic absorption properties of NiZn ferrite in function of the Cu doping (Bueno et al., 2008; Ruiz et al., 2013; Lima et al., 2008; Pessoa et al., 2013).

Comparing the absorption profiles of the NZC2 and NZC2-12 ferrites, it is observed that the ferrite after sintering favored an increase in the reflectivity loss for lower frequencies, that is, the low intensity loss peak (-2.5 dB) in around 11.5 GHz that appears for NZC2 ferrite, after sintering (NZC2-12), pass to extend over the entire frequency range below 11.5 GHz, reaching the maximum value of −4.0 dB at 8.2 GHz (NZC2-12).

For a better comparison between the reflection losses of the studied ferrites, the best result of R_L versus frequency of each ferrite associated to the thickness of best performance was plotted in Fig. 17. Therefore, it can be said that the best thicknesses were between 4 and 4.5 mm, and that the NiZn ferrite doped with 0.3 mol of Cu and sintered at 1200 °C/1 h, that is, the NZC3-12 ferrite, responsible for the largest particle size (376.2 nm), the smallest pore volume (0.006 cm^3/g) and the highest density (5.536 g/cm^3), it also confirms its narrowband electromagnetic absorber characteristic, in the 11.5 GHz frequency band, becoming a promising material for RAM applications.

It is known that multidomains have a greater capacity to absorb electromagnetic radiation due to their greater contribution of domain wall motion, which promotes a greater resonance effect, dissipating energy by means of heat, and therefore, increasing the reflective property of the material (Pessoa et al., 2013; Liu et al., 2017b, 2017c; Yan et al., 2018). Thus, it was expected that the as synthesized ferrites presented limited radiation absorption capacity, since nanometric particles (< 100 nm) do not contribute to domain structures, but rather to coherent rotation behavior, which explains the low magnetization and reflection loss values. Among the as synthesized ferrites, the smallest attenuations presented by the NZ and NZC3 ferrites are possibly related to the interference caused by the presence of the Fe_2O_3 and ZnO segregated phases, which have weak magnetic characteristic. On the other hand, the sintered ferrites, that present particle sizes of 190–376 nm, which suggests the formation of multidomain structures that promote greater domain wall motion, therefore allowing a better magnetic characteristic and, also, a better electromagnetic radiation absorption capacity.

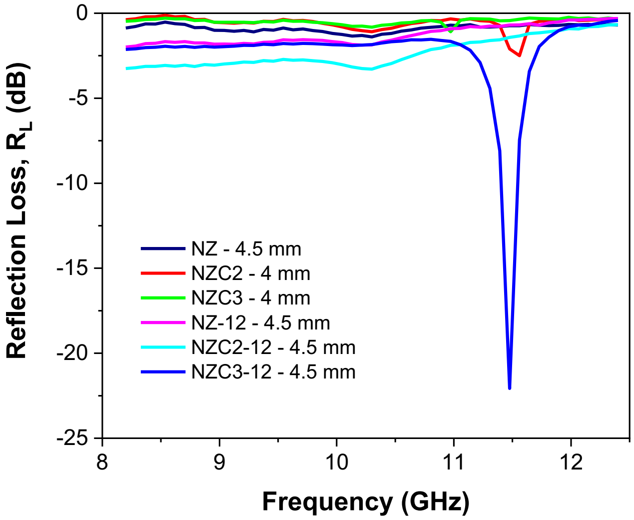

Fig. 17 Measurements of reflection loss (R_L) versus frequency of $Ni_{0.5-x}Zn_{0.5-x}Cu_{2x}Fe_2O_4$ (x = 0; 0.10 and 0.15) ferrites as synthesized and sintered at 1200 °C/1 h.

Lima et al. (2008), when studying $Ni_{0.5-x}Cu_xZn_{0.5}Fe_2O_4$ ferrite nanoparticles (0.2 < x > 0.4) synthesized by the precursor citrate method and sintered at 1100 °C/3 h under argon atmosphere, they observed that the increase in Cu content caused an optimization of radiation absorption at high frequencies, reaching a maximum attenuation of 96.6% at 12 GHz for the concentration of x = 0.4. Dias et al. (2005), when studying electromagnetic radiation absorbing materials based on NiZn ferrite and polyurethane, they achieved 70% attenuation at 12 GHz frequency. Aphesteguy et al. (2009) when studying the $Ni_{0.5}Zn_{0.5}Fe_2O_4$ and $Ni_{0.35}Cu_{0.15}Zn_{0.5}Fe_2O_4$ ferrites synthesized by combustion reaction and sintered at 1000 °C/2 h, they observed R_L values of −3 dB (50%) at 11.7 GHz, and −1 dB (17%) across all the X-band frequency range, respectively. The authors attributed the best attenuation of NiZn ferrite to its lower coercivity (Hc = 6.6 Oe) when compared to that of NiCuZn ferrite (Hc = 20 Oe), stating that the low coercive field favors the electromagnetic radiation absorption, considering that the absorption alters the spin state (magnetization) and facilitates heat dissipation into the material. Comparing these results by Aphesteguy et al. (2009) with those of the sintered ferrites under study, an inverse behavior was observed for coercivity, since the introduction of Cu into NiZn ferrite favored the reduction of coercivity, whose values were 16.42, 1.02 and 2.75 Oe for the NZ-12, NZC2-12 and NZC3-12 ferrites, respectively; however, similar behavior was observed in relation to obtaining the best RL values for the lowest coercivity values. Liu et al. (2017b) also stated that materials with high saturation magnetization associated with low coercivity exhibit strong electromagnetic absorption properties. These reports corroborate, therefore, the promising results achieved by NZC3-12 ferrite in the present study, where structural, textural, morphological and magnetic modifications promoted by the Cu doping into the NiZn ferrite, together with the sintering process, led to the improvement of narrowband electromagnetic absorption properties.

4. Conclusions

The pilot-scale combustion reaction synthesis was successfully performed to obtain the different compositions of $Ni_{0.5\text{-}x}Zn_{0.5\text{-}x}Cu_{2x}Fe_2O_4$ (x = 0; 0.10 and 0.15) ferrites system. The XRD patterns confirmed the formation of the spinel cubic structure as majoritary phase, with the presence of Fe_2O_3 and/or ZnO as segregated phases. The obtaining of the cubic spinel structure in single-phase form was possible after sintering process. The Cu doping into the NiZn ferrite led to a reduction in the combustion synthesis temperature, and, therefore, a decrease in crystallite size, crystallinity and lattice parameter. The oxide compositions confirmed the suggested stoichiometry. The increase in Cu content, due its ease of interdiffusion into the NiZn ferrite structure, allowed for an increase in particle size, a decrease in surface area, a reduction in pore volume and an increase in density, which in turn are important characteristics for RAM application. After sintering, a significant increase in particle size (190.01–376.20 nm) was observed when compared with the as synthesized ferrites (25.93–28.21 nm), enabling the formation of multidomains, and contributing to a better magnetic characteristic. The introduction of Cu favored the reduction of saturation magnetization and coercivity. All ferrites showed a soft ferrimagnetic behavior. The morphological analysis showed significant changes after sintering and doping with Cu, starting to present denser grains and with well-defined polygonal shapes. The best performance of electromagnetic absorption in the X-band was presented by the sintered ferrite with 0.3 mol of Cu (NZC3-12), with 99.8% attenuation in the 11.5 GHz frequency, thus confirming its efficiency and great potential to be applied as a narrowband electromagnetic radiation absorber material.

Declaration of Competing Interest

The authors declare that they have no known competing financial interests or personal relationships that could have appeared to influence the work reported in this paper.

Acknowledgments

The authors are grateful to RENAMI/CNPq-Brazil, CNPq/Multi-user case: (402561/2007-4), PROCAD/NF-CAPES, PRO-Engineering-CAPES, CNPq/CAPES and Homeland Foundation - FINEP-Brazil (Research Project: 400630/2014-1 – MATEST: 01.09.0546.00) for the financial support.

References

Ahmed, T.T., Rahman, I.Z., Rahman, M.A., 2004. Study on the properties of the copper substituted NiZn ferrites. J. Mater. Process. Technol. 153–154, 797–803.

Ali, N.N., Al-Marjeh, R.A.Q.B., Atassi, Y., Salloum, A., Malki, A., Jafarian, M., 2018. Design of lightweight broadband microwave absorbers in the X-band based on (polyaniline/MnNiZn ferrite) nanocomposites. J. Magn. Magn. Mater. 453, 53–61.

Aphesteguy, J.C., Damiani, A., Digiovanni, D., Jacobo, S.E., 2009. Microwave-absorbing characteristics of epoxy resin composites containing nanoparticles of NiZn- and NiCuZn-ferrites. Physica B 404 (18), 2713–2716.

Bajorek, A., Berger, C., Dulski, M., Łopadczak, P., Zubko, M., Prusik, K., Wojtyniak, M., Chrobak, A., Grasset, F., Randrianantoandro, N., 2019. Microstructural and magnetic characterization of $Ni_{0.5}Zn_{0.5}Fe_2O_4$ ferrite nanoparticles. J. Phys. Chem. Solids 129, 1–21.

Baker-Jarvis, J., Janezic, M.D., Grosvenor, J.H., Geyer, R.G., 1993. Transmission/Reflection and Short-Circuit Line Methods for Measuring Permittivity and Permeability, NIST Technical Note 1355-R, Washington.

Barba, A., Clausell, C., Jarque, J.C., Nuño, L., 2020. Magnetic complex permeability (imaginary part) dependence on the microstructure of a Cu-doped Ni-Zn-polycrystalline sintered ferrite. Ceram. Int. 46 (10), 14558–14566.

Bueno, A.R., Gregori, M.L., Nóbrega, M.C.S., 2008. Microwave-absorbing properties of $Ni_{0.50-x}Zn_{0.50-x}Me_{2x}Fe_2O_4$ (Me = Cu, Mn, Mg) ferrite–wax composite in X-band frequencies. J. Magn. Magn. Mater. 320 (6), 864–870.

Caltun, O.F., Spinu, L., Stancu, A., 2001. Magnetic properties of high frequency Ni-Zn ferrites doped with CuO. IEEE Trans. Magn. 37 (4), 2353–2355.

Conkling, J.A., Mocella, C., 2010. Color and light production. Chemistry of Pyrotechnics: Basic Principles and Theory, second ed., Chap. 8, CRC Press, New York, NY, USA, p. 179–202.

Costa, A.C.F.M., Tortella, E., Morelli, M.R., Kiminami, R.H.G.A., 2003. Synthesis microstructure and magnetic properties of Ni-Zn ferrites. J. Magn. Magn. Mater. 256, 174–182.

Costa, A.C.F.M., Kiminami, R.H.G.A., 2012. Dispositivo para produção de nanomateriais cerâmicos em larga escala por reação de combustão e processo contínuo de produção dos nanomateriais. Revista de Propriedade Industrial-RPI, n° BR 25, 002181–002183.

Costa, F., Borgese, M., Degiorgi, M., Monorchio, A., 2017. Electromagnetic characterization of materilas by using transmission/reflection (T/R) devices. Electronics 6. 95(1–27).

Dantas, J., Costa, A.C.F.M., 2019. Escala piloto de produção da Nanoferrita Ni0,5Zn0,5Fe2O4: Avaliação da reprodutibilidade para aplicação como catalisador nanomagnético na obtenção de biodiesel. Petróleo e Outros Combustíveis. 1ª Ed., Editora Poisson, cap. 23, p. 158–187.

Dantas, J., Leal, E., Cornejo, D.R., Kiminami, R.H.G.A., Costa, A.C. F.M., 2020. Biodeisel production evaluating the use and reuse of magnetic nanocatalysts $Ni_{0.5}Zn_{0.5}Fe_2O_4$ synthesized in pilot-scale. Arabian J. Chem. 13 (1), 3026–3042.

Dantas, J., Leal, E., Mapossa, A.B., Cornejo, D.R., Costa, A.C.F.M., 2017. Magnetic nanocatalysts of $Ni_{0.5}Zn_{0.5}Fe_2O_4$ doped with Cu and performance evaluation in transesterification reaction for biodiesel production. Fuel 191, 463–471.

Das, P.S., Singh, G.P., 2016. Structural, magnetic and dielectric study of Cu substituted NiZn ferrite nanorod. J. Magn. Magn. Mater. 401, 918–924.

Deepty, M., Srinivas, C., Kumar, E.R., Mohan, N.K., Prajapat, C.L., Rao, T.V.C., Meena, S.S., Verma, A.K., Sastry, D.L., 2019. XRD, EDX, FTIR and ESR spectroscopic studies of co-precipitated Mn–substituted Zn–ferrite nanoparticles. Ceram. Int. 45, 8037–8044.

Dias, J.C., Martin, I.M., Nohara, E.L., Rezende, M.C., 2005. Refletividade de fótons micro-ondas por tintas poliuretanas aditivadas com ferritas NiZn e MnZn. Revista de Física Aplicada e Instrumentação 18, 24–33.

Dimri, M.C., Verma, A., Kashyap, S.C., Dube, D.C., Thakur, O.P., Prakash, C., 2006. Structural, dielectric and magnetic properties of NiCuZn ferrite grown by citrate precursor method. Mater. Sci. Eng., B 133, 42–48.

Ehi-Eromosele, C.O., Ita, B.I., Iwela, E.E.J., 2015. Low-temperature combustion synthesis of cobalt magnesium ferrite magnetic nanoparticles: effects of fuel-to-oxidizer ratio and sintering temperature. J. Sol-Gel Sci. Technol. 76, 298–308.

Gabal, M.A., Al-Juaid, A.A., 2020. Cr-substitution effect on structural and electromagnetic properties of Mg-Ni ferrite synthesized via sucrose auto-combustion method. J. Alloy. Compd. 813, 152250.

Gao, P., Hua, X., Degirmenci, V., Rooney, D., Khraisheh, M., Pollard, R., Bowman, R.M., Rebrov, E.V., 2013. Structural and magnetic properties of $Ni_{1-x}Zn_xFe_2O_4$ ($x = 0$, 0.5 and 1) nanopowders prepared by sol–gel method. J. Magn. Magn. Mater. 348, 44–50.

Green, M., Chen, X., 2019. Recent progresso f nanomateerials for microwave absorption. J. Materiomics 5, 503–541.

Griffiths, D., 1999. Introduction to Electrodynamics. Cambridge University Press.

Guo, R., Wang, S., Yu, Z., Sun, K., Jiang, X., Wu, G., Wu, C., Lan, Z., 2020. FeSiCr@NiZn SMCs with ultra-low core losses, high resistivity for high frequency applications. J. Alloy. Compd. 830, 154736.

Hajarpour, S., Raouf, A.H., Gheisari, K., 2014. Structural evolution and magnetic properties of nanocrystalline magnesium–zinc soft ferrites synthesized by glycine–nitrate combustion process. J. Magn. Magn. Mater. 363, 21–25.

Hashim, M., Raghasudha, M., Shah, J., Shirsath, S.E., Ravinder, D., Kumar, S., Meena, S.S., Bhatt, P., Alimuddin, Kumarh, R., Kotnala, R.K., 2018. High temperature dielectric studies of indium-substituted NiCuZn nanoferrites. J. Phys. Chem. Solids 112, 29–36.

Hossen, M.B., Hossain, A.K.M.A., 2015. Structural and dynamic electromagnetic properties of $Ni_{0.27}Cu_{0.10}Zn_{0.63}Al_xFe_{2-x}O_4$. J. Magn. Magn. Mater. 387, 24–36.

Houshiar, M., Jamilpanah, L., 2018. Effect of Cu dopant on the structural, magnetic and electrical properties of Ni-Zn ferrites. Mater. Res. Bull. 98, 213–218.

Hwang, C.-C., Tsai, J.-S., Huang, T.-H., Peng, C.-H., Chen, S.-Y., 2005. Combustion synthesis of Ni–Zn ferrite powder—influence of oxygen balance value. J. Solid State Chem. 178 (1), 382–389.

Jafarian, M., Afghahi, S.S.S., Atassi, Y., Salehi, M., 2019. Insights on the design of a novel multicomponent microwave absorber based on $SrFe_{10}Al_2O_{19}$ and $Ni_{0.5}Zn_{0.5}Fe_2O_4$/MWCNTs/polypyrrole. J. Magn. Magn. Mater. 471, 30–38.

Jain, S., Adiga, K., Verneker, V.P., 1981. A new approach to thermochemical calculations of condensed fuel-oxidizer mixtures. Combust. Flame 40, 71–79.

Jia, L., Zhang, H., Wu, X., Li, T., Su, H., Liu, B., 2012. Microstructures and magnetic properties of Bi-substituted NiCuZn ferrite. J. Appl. Phys. 111 (7), 07A326.

Kabbur, S.M., Waghmare, S.D., Nadargi, D.Y., Sartale, S.D., Kambale, R.C., Ghodake, U.R., Suryavanshi, S.S., 2019. Magnetic interactions and electrical properties of Tb^{3+} substituted NiCuZn ferrites. J. Magn. Magn. Mater. 473, 99–108.

Kabbur, S.M., Ghodake, U.R., Nadargi, D.Y., Kambale, R.C., Suryavanshi, S.S., 2018. Effect of Dy^{3+} substitution on structural and magnetic properties of nanocrystalline Ni-Cu-Zn ferrites. J. Magn. Magn. Mater. 451, 665–675.

Klug, H.P., Alexander, L.E., 1954. X-Ray Diffraction Procedures for Polycrystalline and Amorphous Materials. John Wiley and Sons Inc, New York.

Krishna, K.R., Ravinder, D., Kumar, K.V., Lincon, CH.A., 2012. Synthesis, XRD & SEM studies of zinc substitution in nickel ferrites by citrate gel technique. World J. Condens. Matter Phys. 2, 153–159.

Kumar, S., Sharma, A., Singh, M., Sharma, S.P., 2014. Synthesis of magnesium-zinc nano ferrites by using Aloe vera extract solution and their structural and magnetic characterizations. Arch. Phys. Res. 5 (1), 18–24.

Leal, E., Dantas, J., Santos, P.T.A., Bicalho, S.M.C.M., Kiminami, R. H.A.G., Silva, M.R., Costa, A.C.F.M., 2018. Effect of the surface treatment on the structural, morphological, magnetic and biological properties of MFe_2O_4 iron spinels (M = Cu, Ni Co, Mn and Fe). Appl. Surf. Sci. 455, 635–645.

Li, L.-Z., Zhong, X.-X., Wang, R., Tu, X.-Q., He, L., Wang, F.-H., 2019. Effects of Ce substitution on the structural and electromagnetic properties of NiZn ferrite. J. Magn. Magn. Mater. 475, 1–4.

Lima, U.R., Nasar, M.C., Nasar, R.S., Rezende, M.C., Araújo, J.H., Oliveira, J.F., 2008. Synthesis of NiCuZn ferrite nanoparticles and microwave absorption characterization. Mater. Sci. Eng., B 151, 238–242.

Liu, P., Ng, V.M.H., Yao, Z., Zhou, J., Lei, Y., Yang, Z., Kong, L.B., 2017a. Microwave absorption properties of double-layer absorbers based on $Co_{0.2}Ni_{0.4}Zn_{0.4}Fe_2O_4$ ferrite and reduced graphene oxide composites. J. Alloy. Compd. 701, 841–849.

Liu, Q., Huang, H., Lai, L., Sun, J., Shang, T., Zhou, Q., Xu, Z., 2009. Hydrothermal synthesis and magnetic properties of $NiFe_2O_4$ nanoparticles and nanorods. J. Mater. Sci. 44, 1187–1191.

Liu, S., Wei, K., Cheng, Y., Yan, S., He, L., Deng, L., 2019. Structural, magnetic and microwave electromagnetic properties in La-substituted quaternary ferrite. J. Alloy. Compd. 791, 469–476.

Liu, Z., Che, R., Wei, Y., Liu, Y., Elzatahry, A.A., Dahyan, D.A., Zhao, D., 2017b. Broadening microwave absorption via multi-domain structure. APL Mater. 5, 046104.

Liu, Z., Peng, Z., Lv, C., Fu, X., 2017c. Doping effect of Sm^{3+} on magnetic and dielectric properties of Ni-Zn ferrites. Ceram. Int. 43 (1), 1449–1454.

Lv, H., Rebrov, E.V., Gao, P., Ma, R., Lu, Z., Xu, J., 2016. Controllable synthesis of one-dimensional isolated $Ni_{0.5}Zn_{0.5}Fe_2O_4$ microtubes for application as catalyst support in RF heated reactors. Ceram. Int. 42 (6), 7793–7802.

Mapossa, A.B., Dantas, J., Silva, M.R., Kiminami, R.H.G.A., Costa, A.C.F.M., Daramola, M.O., 2020. Catalytic performance of $NiFe_2O_4$ and $Ni_{0.3}Zn_{0.7}Fe_2O_4$ magnetic nanoparticles during biodiesel production. Arabian J. Chem. 13 (2), 4462–4476.

Melvin, G.J.H., Ni, Q.Q., Suzuki, Y., Natsuki, T., 2014. Microwave-absorbing properties of silver nanoparticle/carbon nanotube hybrid nanocomposites. J. Mater. Sci. 49, 5199–5207.

Naidu, K.C.B., Roopaskiran, S., Madhuri, W., 2017. Investigations on transport, impedance and electromagnetic interference shielding properties of microwave processed NiMg ferrites. Mater. Res. Bull. 89, 125–138.

Nakamura, T., Okano, Y., 1997. Low temperature sintered Ni-Zn-Cu ferrite. Journal de Physique IV Colloque 07 (C1), C191–C192.

Nam, J.-H., Park, S.J., Kim, W.K., 2003. Microstructure and magnetic properties of nanostructured NiZnCu ferrite powders synthesized by sol-gel process. IEEE Trans. Magn. 39 (5), 3139–3141.

Nicolson, A.M., 1968. Broad-band microwave transmission characteristics from a single measurement of the transient response. IEEE Trans. Instrum. Meas. 17 (4), 395–402.

Oliveira, D.M., Andrada, A.S., 2019. Synthesis of ordered mesoporous silica MCM-41 with controlled morphology for potential application in controlled drug delivery systems. Cerâmica 65, 170–179.

Parfenov, V.V., Roumaih, K.M., Manapov, R.A., Ibragimov, SH.Z., 2003. Effects of cation distribution and oxidation state on the electrical and magnetic properties of $Ni_{1-x}Cu_xFeMnO_4$. Inorg. Mater. 39 (12), 1315–1319.

Peng, Y., Yi, Y., Li, L., Ai, H., Wang, X., Chen, L., 2017. Fe-based soft magnetic composites coated with NiZn ferrite prepared by a co-precipitation method. J. Magn. Magn. Mater. 428, 148–153.

Peng, Z.J., Fu, X.L., Ge, H.L., Fu, Z.Q., Wang, C.B., Qi, L.H., Miao, H.Z., 2011. Effect of Pr^{3+} doping on magnetic and dielectric properties of Ni–Zn ferrites by "one-step synthesis". J. Magn. Magn. Mater. 323, 2513–2518.

Pereira, S.L., Pfannes, H.-D., Mendes Filho, A.A., Miranda Pinto, L. C.B., Chíncaro, M.A., 1999. A comparative study of NiZn ferrites modified by the addition of cobalt. Mater. Res. 2 (3), 231–234.

Pessoa, R.C., Nasar, M.C., Nasar, R.S., Rezende, M.C., Hwang, M. K., 2013. Attenuation of incident radiation in composite of NiZn ferrite doped with magnesium and copper in epoxy. Cerâmica 59, 59–64.

Pozo López, G., Silvetti, S.P., Urreta, S.E., Carreras, A.C., 2010. Structure and magnetic properties of NiZn ferrite/SiO_2 nanocomposites synthesized by ball milling. J. Alloys Compounds 505 (2), 808–813.

Praveena, K., Sadhana, K., Liu, H.L., Maramu, N., Himanandini, G., 2016. Improved microwave absorption properties of TiO_2 and $Ni_{0.53}Cu_{0.12}Zn_{0.35}Fe_2O_4$ nanocomposites potential for microwave devices. J. Alloy. Compd. 681, 499–507.

Praveena, K., Sadhana, K., Virk, H.S., 2015. Structural and magnetic properties of Mn-Zn ferrites synthesized by microwave-hydrothermal process. Solid State Phenom. 232, 45–64.

Qin, F., Brosseau, C., 2012. A review and analysis of microwave absorption in polymer composites filled with carbonaceous particles. J. Appl. Phys. 111, 061301.

Qinghui, Y., Huaiwu, Z., Yingli, L., Qiye, W., Lijun, J., 2012. Microstructure and magnetic properties of microwave sintered NiCuZn ferrite for application in LTCC devices. Mater. Lett. 79, 103–105.

REED, J.S., 1995. Principles of Ceramics Processing. John Wiley & Sons Inc., New York, NY, USA.

Rezlescu, E., Sachelarie, L., Popa, P.D., Rezlescu, N., 2000. Effect of substitution of divalent ions on the electrical and magnetic properties of Ni-Zn-Me ferrites. IEEE Trans. Magn. 36 (6), 3962–3967.

Ruiz, M.S., Bercoff, P.G., Jacobo, S.E., 2013. Shielding properties of CuNiZn ferrite in the radio frequency range. Ceram. Int. 39 (5), 4777–4782.

Satpute, S.S., Wadgane, S.R., Kadam, S.R., Mane, D.R., Kadam, R. H., 2019. Y^{3+} substituted Sr-hexaferrites: sol-gel synthesis, structural, magnetic and electrical characterization. Cerâmica 65, 274–281.

Sing, K., Everett, D., Haul, R., Moscou, L., Pierotti, R., Rou-Querol, J., Siemieniewska, T., 1985. Reporting physisorption data for gas/solid systems - with special reference to the determination of surface area and porosity. Pure Appl. Chem. (IUPAC) 57, 603–619.

Slimani, Y., Unal, B., Almessiere, M.A., Korkmaz, A.D., Shirsath, S. E., Yasin, G., Trukhanov, A.V., Baykal, A., 2020. Investigation of structural and physical properties of Eu^{3+} ions substituted $Ni_{0.4}Cu_{0.2}Zn_{0.4}Fe_2O_4$ spinel ferrite nanoparticles prepared via sonochemical approach. Results Phys. 17, 103061.

Sugimoto, M., 1999. The past, present, and future of ferrites. J. Am. Ceram. Soc. 82 (2), 269–280.

Sujatha, C., Reddy, K.V., Babu, K.S., Reddy, A.R., Rao, K., 2013. Effect of sintering temperature on electromagnetic properties of NiCuZn ferrite. Ceram. Int. 39 (3), 3077–3086.

Tsay, C., Liu, K., Lin, T., Lin, I., 2000. Microwave sintering of NiCuZn ferrites and multilayer chip inductors. J. Magn. Magn. Mater. 209 (1–3), 189–192.

Venkatesh, D., Ramesh, K.V., 2017. Structural and electrical properties of Cu-doped Ni-Zn nanocrystalline ferrites for MLCI applications. Mod. Phys. Lett. B 31 (33), 1750318–1750333.

Venkatesh, D., Vara-Prasad, B.B.V.S., Ramesh, K.V., Ramesh, M.N. V., 2020. Magnetic properties of Cu^{2+} substituted Ni–Zn nanocrystalline ferrites synthesized in citrate-gel route. J. Inorg. Organ. Polym. Mater. 30, 2057–2066.

Virlan, C., Tudorache, F., Pui, A., 2020. Tertiary NiCuZn ferrites for improved humidity sensors: a systematic study. Arabian J. Chem. 13 (1), 2066–2075.

Wang, M., Wang, Z., Wang, P., Liao, Y., Bi, H., 2017. Single-layer and double-layer microwave absorbers based on $Co_{67}Ni_{33}$ microspheres and $Ni_{0.6}Zn_{0.4}Fe_2O_4$ nanocrystals. J. Magn. Magn. Mater. 425, 25–30.

Yan, S., Geng, J., Yin, L., Zhou, E., 2004. Preparation of nanocrystalline NiZnCu ferrite particles by sol–gel method and their magnetic properties. J. Magn. Magn. Mater. 277 (1–2), 84–89.

Yan, S., Liu, S., He, J., Luo, H., He, L., Li, Y., Huang, S., Deng, L., 2018. Effects of Co_2O_3 on electromagnetic properties of NiCuZn ferrites. J. Magn. Magn. Mater. 452, 349–353.

Zhao, S., Wang, C., Zhong, B., 2020. Optimization of electromagnetic wave absorbing properties for Ni-Co-P/GNs by controlling the content ratio of Ni to Co. J. Magn. Magn. Mater. 495, 165753.

Zhou, J., Shu, X., Wang, Y., Ma, J., Liu, Y., Shu, R., Kong, L., 2020. Enhanced microwave absorption properties of $(1\text{-}X)CoFe_2O_4/_X$-CoFe composites at multiple frequency bands. J. Magn. Magn. Mater. 493, 165699.

Zhou, X., Zhou, Y., Zhou, L., Wei, J., Wu, J., Yao, D., 2019. Effect of Gd and La doping on the structure, optical and magnetic properties of NiZnCo ferrite. Ceram. Int. 45, 6236–6242.